CrossMark

The Diverse Shapes of Dwarf Planet and Large KBO Phase Curves Observed from New Horizons

Anne J. Verbiscer[1], Paul Helfenstein[2], Simon B. Porter[3], Susan D. Benecchi[4], J. J. Kavelaars[5], Tod R. Lauer[6], Jinghan Peng[7], Silvia Protopapa[3], John R. Spencer[3], S. Alan Stern[3], Harold A. Weaver[8], Marc W. Buie[3], Bonnie J. Buratti[9], Catherine B. Olkin[3], Joel Parker[3], Kelsi N. Singer[3], and Leslie A. Young[3]

The New Horizons Science Team

[1] Department of Astronomy, University of Virginia, P.O. Box 400325, Charlottesville, VA 22904-4325, USA; av4n@virginia.edu
[2] Department of Astronomy, 404 Space Sciences Building, Cornell University, Ithaca, NY 14853, USA
[3] Southwest Research Institute, 1050 Walnut Street, Suite 300, Boulder, CO 80302, USA
[4] Planetary Science Institute, 1700 East Fort Lowell, Suite 106, Tucson, AZ 85719, USA
[5] Herzberg Astronomy and Astrophysics Research Centre, National Research Council of Canada, 5071 West Saanich Road, Victoria, BC V9E 2E7, Canada
[6] NSF's National Optical Infrared Astronomy Research Laboratory, 950 North Cherry Avenue, Tucson, AZ 85719, USA
[7] Department of Physics and Astronomy, University of Victoria, PO Box 1700 STN CSC, Victoria, BC V8W 2Y2, Canada
[8] The Johns Hopkins University Applied Physics Laboratory, 11100 Johns Hopkins Road, Laurel, MD 20723, USA
[9] Jet Propulsion Laboratory, 4800 Oak Grove Drive, Pasadena, CA 91109, USA
Received 2021 July 30; revised 2022 March 29; accepted 2022 March 30; published 2022 April 27

Abstract

Observing dwarf planets and other large Kuiper Belt objects (KBOs) from vantage points between 8 and 47 au from the Sun, NASA's New Horizons spacecraft has found diversity in the shapes of their solar phase curves. Here we extend solar phase angle coverage of dwarf planets (136199) Eris, (136472) Makemake, and (136108) Haumea; large KBOs (28978) Ixion, (50000) Quaoar, (307261) 2002 MS$_4$, and (556416) 2014 OE$_{394}$; and Neptune's satellite Triton to phase angles as high as $\alpha = 94°$ using New Horizons data and fit the resulting solar phase curves to the Hapke photometric model. When accounting for sparse α sampling, these fits yield large uncertainties in the Hapke parameters; however, opposition effect parameters are generally well constrained and suggest a significant range of regolith maturation ages among these bodies. The expanded range in α enables evaluation of Bond albedos, phase integrals, rotation curves at high α, and comparisons of the surface scattering properties of these objects with those of others in the solar system. The dwarf planets with surface compositions dominated by hypervolatiles, Eris and Makemake, and Triton (a likely former KBO) have shallower solar phase curve slopes (i.e., lower phase coefficients, higher phase integrals, and Bond albedos) than objects with volatile-poor surfaces. The total amplitude of Haumea's rotation curve at $\alpha = 48°$ is $\Delta m = 0.6 \pm 0.2$ mag, nearly twice that of its rotation curve measured from Earth at low phase angles. Bond albedos range from 0.037 ± 0.007 for Ixion to $0.99^{+0.01}_{-0.09}$ for Eris.

Unified Astronomy Thesaurus concepts: Planetary surfaces (2113); Kuiper belt (893); Surface photometry (1670)

1. Introduction

According to the International Astronomical Union (IAU), five objects in the solar system are classified as dwarf planets (DPs): (1) Ceres, (134340) Pluto, (136108) Haumea, (136199) Eris, and (136472) Makemake. One, Ceres, orbits the Sun in the main asteroid belt between Mars and Jupiter, and the other four orbit the Sun beyond Neptune, although at perihelion Pluto is briefly closer to the Sun than Neptune.

Since 2007, just over 1 yr after launch, NASA's New Horizons spacecraft has been measuring the photometric behavior of all DPs (except Ceres) and other "distant" Kuiper Belt objects (DKBOs; Porter et al. 2016; Verbiscer et al. 2019b) from its unique vantage point beyond Jupiter initially and now from within the Kuiper Belt. New Horizons also observed Triton, Neptune's largest satellite and a body larger than Pluto that likely was once a Kuiper Belt object (KBO; Agnor & Hamilton 2006), from multiple viewing geometries unattainable from Earth. The objectives of New Horizons' Kuiper Belt exploration include measuring how DP and DKBO reflectance varies with rotation from different viewing geometries to determine their rotation rates and pole positions and to constrain their shapes. Another primary objective is to construct DP and DKBO solar phase curves, measurements of how their reflectance varies with solar phase (Sun−target−observer) angle α.

The size of Earth's orbit restricts solar phase angle coverage for Earth-based observations of many solar system objects, even main belt asteroids. Spacecraft passing through the asteroid belt (e.g., Galileo, Deep Space 1) and missions to small bodies (e.g., Near Earth Asteroid Rendezvous—Shoemaker (NEAR), Stardust), however, have expanded phase angle coverage for asteroids and Jupiter-family comets (JFCs). Likewise, outer solar system missions such as Voyager, Galileo, and Cassini have expanded the phase angle coverage for the satellites of the giant planets. While Earth-based observations of solar system objects beyond the orbit of Neptune are limited to phase angles $\alpha < 2°$, the analysis of their solar phase curves near opposition has nevertheless revealed correlations between the phase coefficient β, or slope of the phase curve, and dynamical class, as well as a wavelength dependence of β on dynamical class (e.g., Rabinowitz et al. 2007; Schaefer et al. 2009; Verbiscer et al. 2013).

Table 1
Orbital Elements, Dynamical Class, and Absolute Magnitudes H_V of Dwarf Planets, Satellites, and Large KBOs Observed by New Horizons

Object	Dynamical Class[a]	A[b] (au)	Eccentricity e	Inclination i (deg)	q[b] (au)	Q[b] (au)	Absolute Magnitude H_V	References
Eris	Detached	67.9	0.436	44.04	38.3	97.5	-1.124 ± 0.025	1
Makemake	Classical	45.4	0.161	28.98	38.1	52.8	0.049 ± 0.020	2
Haumea	Resonant (7:12)	43.2	0.195	28.21	34.8	51.6	0.358 ± 0.011[c]	3
Quaoar	Classical	43.7	0.041	7.99	41.9	45.5	2.737 ± 0.008	4
2002 MS$_4$	Classical	42.0	0.139	17.68	36.2	47.9	4.0 ± 0.6	5
Ixion	Resonant (3:2)	39.8	0.246	19.60	30.0	49.6	3.774 ± 0.021	1
2014 OE$_{394}$	Classical	46.2	0.118	3.94	40.8	52.0	4.8	6
Triton[d]	Satellite	30.1	0.009	1.77	29.8	30.33	-1.2	7
Pluto	Resonant (3:2)	39.5	0.249	17.16	29.7	49.3	-0.881 ± 0.400	8
Charon	Resonant (3:2)	39.5	0.249	17.16	29.7	49.3	1	7

Notes.
[a] Classifications according to Gladman et al. (2008).
[b] A, q, and Q are the semimajor axis, perihelion distance, and aphelion distance, respectively, in astronomical units (au).
[c] H_V magnitude of the Haumea system in 2017 (Ortiz et al. 2017), including its satellites and ring. The Haumea system's H_V magnitude changes as a function of its projected area viewed from Earth or New Horizons. In 2005, Rabinowitz et al. (2007) measured $H_V = 0.428 \pm 0.011$ for the Haumea system.
[d] Orbital parameters given for Triton are those of Neptune.

References. (1) Alvarez-Candal et al. 2016; (2) Hromakina et al. 2019; (3) Ortiz et al. 2017; (4) http://www2.lowell.edu/users/grundy/tnbs/50000_2002_LM60_Quaoar.html; (5) Vilenius et al. 2012; (6) JPL Small Body Database; (7) Howett et al. 2021; (8) Hainaut et al. 2012.

Table 2
Size, Albedo, Colors, and Surface Composition of Dwarf Planets, Satellites, and Large KBOs Observed by New Horizons

Object	Diameter (km)	Geometric Albedo p_V	Color $B - V$ (mag)	Color $V - R$ (mag)	Primary Surface Composition	References
Eris	2326	$0.96^{+0.09}_{-0.04}$	0.805 ± 0.015	0.389 ± 0.049	CH_4, N_2	1–5
Makemake	1434×1420	0.82 ± 0.02	0.828 ± 0.022	0.437 ± 0.02	CH_4, C_2H_6	2, 6–8
Haumea[a]	$2100 \times 1680 \times 1074$	0.66 ± 0.02	0.631 ± 0.025	0.370 ± 0.020	H_2O	2,9,10
Quaoar	1138×1036	0.109 ± 0.007	0.939 ± 0.008	0.65 ± 0.01	H_2O	2,11,12
2002 MS$_4$	808×748	0.098 ± 0.004	0.69 ± 0.02	0.38 ± 0.02	unknown	13,14
Ixion	757×685	0.108 ± 0.002	1.03 ± 0.03	0.61 ± 0.03	amorphous C	15–19
2014 OE$_{394}$[b]	304–486	$0.15^{+0.08}_{-0.06}$	0.996 ± 0.140	0.630 ± 0.086	unknown	2,20
Triton	2706.8	0.86 ± 0.004	0.791 ± 0.002	0.608 ± 0.002	N_2, CH_4	21,22
Pluto	2376.6	0.51 ± 0.01	0.954 ± 0.001	0.515 ± 0.035	N_2, CH_4	2,23–26
Charon	1212	0.41 ± 0.01	0.7315 ± 0.0013	0.4	H_2O	24,25

Notes.
[a] For Haumea, the geometric albedo is the geometric albedo of Haumea alone, $p_v = 0.66$, determined by Dunham et al. (2019) from their analysis of stellar occultation results reported by Ortiz et al. (2017), and color indices are those of the Haumea system, including its satellites and ring (Hainaut et al. 2012).
[b] For 2014 OE$_{294}$, the size range is commensurate with the H_V magnitudes assuming the average geometric albedo $p_V = 0.15^{+0.08}_{-0.06}$ for CCKBOs from Lacerda et al. (2014), and its color indices are assumed to match those of other CCKBOs measured by Hainaut et al. (2012).

References. (1) Sicardy et al. 2011; (2) Hainaut et al. 2012; (3) Dumas et al. 2007; (4) Merlin et al. 2009; (5) Alvarez-Candal et al. 2011; (6) Ortiz et al. 2012; (7) Hromakina et al. 2019; (8) Brown et al. 2007a; (9) Dunham et al. 2019; (10) Barkume et al. 2006; (11) Braga-Ribas et al. 2013; (12) http://www2.lowell.edu/users/grundy/tnbs/50000_2002_LM60_Quaoar.html; (13) Rommel et al. 2020; (14) Tegler et al. 2016; (15) Levine et al. 2021; (16) Doressoundiram et al. 2007; (17) Licandro et al. 2002; (18) Boehnhardt et al. 2004; (19) Barkume et al. 2008; (20) Lacerda et al. 2014; (21) Buratti et al. 2011; (22) Cruikshank et al. 1993; (23) Nimmo et al. 2017; (24) Stern et al. 2015; (25) Buie et al. 2010; (26) Protopapa et al. 2017.

New Horizons observations potentially span nearly the full range of solar phase angles, with the viewing geometry limited only by flight rules that prohibit pointing its imagers close to the Sun, i.e., at $\alpha > 170°$.

Here we present New Horizons observations of three confirmed DPs: Eris, Makemake, and Haumea; three likely DPs, (50000) Quaoar, (28978) Ixion, and (307261) 2002 MS$_4$; Triton; and a large, cold classical KBO (CCKBO) that may possibly be classified as a DP, (556416) 2014 OE$_{394}$. We also reanalyze previously published solar phase curves of Pluto and Charon (Verbiscer et al. 2019a; Hillier et al. 2021; Howett et al. 2021; Olkin et al. 2021) and compare the results to those of the

same analyses of other DPs and large KBOs. Table 1 lists the orbital elements, dynamical class, and absolute magnitudes H_V for all these objects; Table 2 provides their size, visible geometric albedo, and colors. Although the size of 2014 OE$_{394}$ has not yet been measured, either from its radiometric thermal emission or by a stellar occultation, its low H_V magnitude ($H_V \sim 5$) suggests that it may be a large KBO, possibly a DP candidate, assuming that its albedo is similar to that of other CCKBOs.

Earth-based observations of Pluto, Charon, and Triton during node crossings presented the opportunity to measure their geometric albedos at the minimum solar phase angle at

which these objects can be observed, defined by the angular size of the solar radius viewed from each object. Although the angular radius of the Sun viewed from Pluto is $\alpha = 0°0089$, even smaller phase angles are accessible owing to solar limb darkening; therefore, the smallest phase angle at which Pluto and Charon have been observed is $\alpha = 0°0049$ (Verbiscer et al. 2019a). For Triton the smallest phase angle at which it has been observed is $\alpha = 0°0022$ (Buratti et al. 2011). The other objects in this study have not yet been observed during node crossings, so the minimum solar phase angles at which they have been observed are larger ($0°03 \leqslant \alpha \leqslant 0°5$). Their geometric albedos must therefore be estimated using extrapolation to the reflectance at zero phase, or opposition. The visible geometric albedos in Table 2 for Eris, Makemake, Haumea, Quaoar, 2002 MS$_4$, and Ixion may be underestimated as a result. Haumea and Makemake, in particular, may have underestimated geometric albedos because they have not been observed at $\alpha < 0°5$, while the geometric albedos of Ixion, Eris, and Quaoar are less likely to be underestimates because they have been observed at phase angles as small as $\alpha = 0°03$, $0°14$, and $0°17$, respectively.

By combining Earth-based observations obtained at lower solar phase angles (summarized in Table 3) with New Horizons LORRI observations acquired at higher solar phase angles, we construct the first solar phase curves of these DPs and large KBOs with phase angle coverage that extends beyond the maximum $\alpha \sim 2°$ available from Earth. Although Voyager 2 measured Triton's full disk-integrated solar phase curve (Hillier et al. 1990, 1991a), New Horizons LORRI provided additional observations at solar phase angles unattainable from Earth, which we use to reanalyze Triton's solar phase curve and compare it to those of the DPs and large DKBOs.

We also present the first rotation curves at high solar phase angles for these large DKBOs and DPs. Solar phase curves for Makemake, Haumea, and Quaoar have been previously published (Rabinowitz et al. 2007; Heinze & de Lahunta 2009; Hromakina et al. 2019), but never with phase angle coverage extending beyond $\alpha = 1°5$. For these KBOs and 2002 MS$_4$, these are the first solar phase curves with phase angle coverage that extends beyond $\alpha = 2°$. A solar phase curve for 2014 OE$_{394}$ has not been previously published.

While Eris, Makemake, Haumea, and Quaoar all have satellites, Ixion, 2002 MS$_4$, and 2014 OE$_{394}$ have no currently known secondaries. Because New Horizons LORRI cannot resolve any of these system components, we use only Earth-based observations in our analyses that do not resolve the moons, rather than observations from the Hubble Space Telescope (HST), which can resolve these satellite systems, in our construction of rotation and solar phase curves. Unlike Haumea's two satellites, the moons of Eris, Makemake, and Quaoar are dark relative to the primary; therefore, they contribute only a small fraction to the total flux. Section 2.3 discusses the contributions of Haumea's ring and satellites to its total flux in more detail.

In a previous paper, Verbiscer et al. (2019b) presented solar and rotation curves for six smaller DKBOs ($H_V > 6$) observed by New Horizons prior to the 2019 January 1 (486958) Arrokoth flyby; subsequent papers will present solar and rotation curves from other small DKBOs observed after 2018 September. Here we focus on the photometric and surface properties derived from the construction and analysis of the most complete DP and large KBO solar phase curves enabled by New Horizons observations.

2. Observations

New Horizons uses its LOng Range Reconnaissance Imager (LORRI; Cheng et al. 2008; Weaver et al. 2020) to investigate the photometric properties of DPs and KBOs. LORRI is a 20.8 cm aperture, $f/12.6$ Ritchey–Chrétien optical telescope mounted in a fixed position on the New Horizons spacecraft. It has a $0°29$ ($1044''$) field of view, coupled with a back-illuminated CCD with 1024×1024 illuminated pixels. LORRI has no filters, and its bandpass ranges from 350 to 850 nm, with a pivot wavelength at 607.6 nm (Weaver et al. 2020). Although LORRI's native pixel resolution is $1''$ pixel^{-1}, all observations presented here were binned 4×4 to 256×256 pixels with $4''$ pixel^{-1} on-chip resolution. Because New Horizons does not have reaction wheels, all pointing must be done using the spacecraft's thrusters. These thrusters maintain pointing stability within about $3''5$; thus, the 4×4 images are only slightly reduced in actual resolution compared to that of 1×1 images with long exposures. Binned images require far less data volume than unbinned images, reducing downlink time from the spacecraft, which is currently at a light-travel time of more than 6 hr from Earth.

All LORRI observations of DPs and DKBOs acquired prior to 2017 December used exposure times of 10 s. A few experimental images taken in 2017 September and 2019 September demonstrated that the spacecraft has sufficient attitude stability and flight software updates to permit LORRI observations using exposure times as long as 30 and 65 s. Between 2017 December and 2019 December, most DKBO 4×4 images were acquired using 30 s exposures, improving the sensitivity of LORRI by a factor of $2-3$ compared to previous limits using 10 s exposures. Since 2019 December, LORRI exposure times for DKBOs increased again for most DKBOs to 65 s. LORRI's sensitivity is such that DKBOs must have apparent magnitude $V < 21$ in order to be detected by the imager. Typically, LORRI DKBO observations consist of sequences, or "visits," of exposures at a fixed R.A.–decl. pointing. The number of images in each visit varies depending on the apparent magnitude of the DKBO seen by LORRI, and, as of 2019 December, each visit requires fewer 65 s exposures to match or exceed the signal-to-noise ratio achieved previously using 10 and 30 s exposures. Without a dense background star field and viewing at solar elongations $>90°$, the limiting magnitude of 10 and 30 s LORRI exposures is $V \approx 20$ and $V \approx 21$, respectively. The image reduction techniques used here are explained in detail by Porter et al. (2018). The reduction pipeline is an updated version of the one used in the first analysis of LORRI images of a DKBO, Plutino (15810) Arawn, described by Porter et al. (2016), and the one used by Verbiscer et al. (2019b) in their subsequent analysis of Arawn and five other DKBOs observed by New Horizons.

The LORRI DN s^{-1} fluxes convert approximately to a Johnson V magnitude (recall that LORRI is an unfiltered CCD) using

$$V_{\text{LORRI}} = -2.5 \log_{10}(\text{DN s}^{-1}) + 18.94 + \text{CC}, \qquad (1)$$

where CC is a color correction applied to each DP or DKBO provided by Weaver et al. (2020). This equation includes the same zero-point (18.94) for LORRI 4×4 images used by Verbiscer et al. (2019b) in their analysis of smaller DKBOs observed by New Horizons. Uncertainties in New Horizons LORRI photometry are on the order of 2%, based on

Table 3
Summary of Previous Visible Earth-based Observations of Dwarf Planets, Satellites, and Large KBOs Observed by New Horizons

Object	Obs Dates.	Phase Angle α Range (deg)	Phase Coefficient β (V mag deg^{-1})	Rotation Curve Amplitude[a] (V mag)	Rotation Period (hr)	References
Eris	2005–2006	0.16–0.60	0.105 ± 0.020	…	…	1
	2005	0.45–0.47	…	0.05 ± 0.01	>120	2
	2005–2007	0.14–0.58	…	0.01 ± 0.01[b]	14, 28, or 32	3
	2005	0.19–0.45	0.09 ± 0.03[b]	<0.1[b]	…	4
	2005	0.4	…	0.05	3.55	5
	2006	0.15–0.51	0.08 ± 0.03[b]	…	…	6
	2006–2007	…	…	0.1[c]	25.92 ± 0.48	7
	2006–2007	0.16, 0.29	…	…	…	8,9
	2011–2015	0.15–0.60	0.119 ± 0.056	0.10	…	10
	2015–2016	…	…	0.06	349.44 ± 2.4	11
Makemake	2005	0.69–1.14	0.054 ± 0.019	…	…	1
	2007	0.59–0.84	0.037 ± 0.013	0.0286 ± 0.0016	7.7700 ± 0.0030	12
	2005–2007	…	…	0.014 ± 0.002	7.65	13
	2006–2007	…	…	0.03 ± 0.01	22.48	14
	2011–2015	0.5–1.1	0.202 ± 0.015	…	…	9
	2006–2017	0.5–1.1	0.027 ± 0.011[c]	0.032 ± 0.005	22.8266 ± 0.0001	15
Haumea	2005	0.51–1.11	0.110 ± 0.014	0.28 ± 0.04	3.9154 ± 0.0001	1,16
	2007	…	…	0.29 ± 0.02	3.9154 ± 0.0002	17
	2007	…	…	0.28 ± 0.02	3.9153	13
	2009	…	…	0.320 ± 0.006[d]	3.91531 ± 0.00005	18
	2017	…	…	0.25 ± 0.02	3.915341 ± 0.000005	19,20
Quaoar	2003	0.17–1.31	0.159 ± 0.027	0.18 ± 0.10	8.839992	1
	2003	0.2	…	0.3	18.84	5
	2003	…	…	0.133 ± 0.028	17.6788 ± 0.0004	21
	2003, 2011	…	…	0.112 ± 0.011	8.841 ± 0.002	22
	2011–2015	0.17–1.3	0.117 ± 0.221	…	…	10
2002 MS$_4$	2005	0.39	…	…	…	23
	2005, 2011	…	…	0.05 ± 0.01	7.33	22
	2013	0.567, 0.915	…	…	…	10
	2013–2014	0.367–1.218	…	…	…	24
Ixion	2001	1.3	…	…	…	25
	2002	0.25–1.34[b]	…	…	…	26
	2003	0.03–1.32	0.133 ± 0.043	…	…	1
	2007	0.9	…	…	…	8
	2010	>0.02	0.201 ± 0.014	0.06 ± 0.03	15.9 ± 0.5	27
	2010			<0.1	12.4 ± 0.3	28
	2011–2015	0.03–1.3	0.194 ± 0.031	…	…	10
2014 OE$_{394}$	2011–2015	0.137–1.215	…	…	…	29
Triton	2000–2004	0.0022–1.26	0.025 ± 0.005	0.052 ± 0.003	141.04	30
Pluto	2002–2003	0.32–1.73	0.0355 ± 0.0045	0.1798 ± 0.0009	153.29	31
	2015–2019	0.0049–1.74	0.0348 ± 0.0020	0.142 ± 0.002		32
Charon	2002–2003	0.32–1.73	0.123	0.08	153.29	31
	2015–2019	0.0049–1.74	0.123	…	…	32

Notes.
[a] All rotation curves are single peaked with total amplitude A, except for the Haumea system, which has a double-peaked rotation curve.
[b] R-band observations.
[c] B-band observations.
[d] Total amplitude of Haumea's rotation curve without its satellites, measured from HST, which could resolve the full system (Lockwood et al. 2014).

References. (1) Rabinowitz et al. 2007; (2) Carraro et al. 2006; (3) Duffard et al. 2008; (4) Sheppard 2007; (5) Lin et al. 2007; (6) Belskaya et al. 2008; (7) Roe et al. 2008; (8) DeMeo et al. 2009; (9) Merlin et al. 2009; (10) Alvarez-Candal et al. 2016; (11) Holler et al. 2020; (12) Heinze & de Lahunta 2009; (13) Thirouin et al. 2010; (14) Dumas et al. 2007; (15) Hromakina et al. 2019; (16) Rabinowitz et al. 2006; (17) Lacerda et al. 2008; (18) Lockwood et al. 2014; (19) Ortiz et al. 2017; (20) Lellouch et al. 2010; (21) Ortiz et al. 2003; (22) Thirouin 2013; (23) Tegler et al. 2016; (24) Peng et al. 2020; (25) Doressoundiram et al. 2002; (26) Boehnhardt et al. 2004; (27) Rousselot & Petit 2010; (28) Galiazzo et al. 2016; (29) this work; (30) Buratti et al. 2011; (31) Buie et al. 2010; (32) Verbiscer et al. 2019a.

Table 4
LORRI Observations of Dwarf Planet (136199) Eris

Observation Mid-time	r (au)	Δ (au)	α (deg)	Exposure Time (s)	Total Images	LORRI Magnitude	V Magnitude at 1 au[a]
2020-05-27 14:34	95.980	112.189	24.788	64.967	60	19.615 ± 0.137	-0.560
2020-05-29 14:34	95.979	112.197	24.796	64.967	60	19.438 ± 0.115	-0.737
2020-05-31 14:27	95.979	112.204	24.803	64.967	60	19.508 ± 0.119	-0.667
2020-05-29 14:34	95.979	112.197	24.796	64.967	180	19.513 ± 0.081	-0.662[b]

Notes.
[a] Since Eris's color over the LORRI bandpass (350–850 nm) is similar to that of Charon (Table 2), we apply the Weaver et al. (2020) Charon color correction, -0.014 mag, to transform LORRI magnitudes to the Johnson V magnitude of Eris viewed at 1 au from the Sun and 1 au from LORRI.
[b] Entry below the horizontal line is the mean observational circumstances of all LORRI observations of Eris in 2020 May and the magnitude of the stack of 180 LORRI images.

calibration with images of the well-characterized open cluster M7/NGC 6475 (Weaver et al. 2020). The color corrections CC introduce some additional uncertainty because they depend on the degree to which the target's spectrum matches that of the model spectrum used to derive the correction. See Weaver et al. (2020) for additional discussion of LORRI calibration. The following subsections discuss the color corrections CC used in Equation (1) for each target.

2.1. Dwarf Planet (136199) Eris

DP (136119) Eris (2003 UB$_{313}$) was discovered in 2005 as part of the Caltech Wide Area Sky Survey (Trujillo & Brown 2003) using the Palomar-QUEST large-area CCD camera (Rabinowitz et al. 2003) on the Samuel Oschin Schmidt (1.2 m) telescope at Mt. Palomar (Brown et al. 2005b). Eris is the most massive and second largest ($D \sim 2326$ km; Sicardy et al. 2011) of the known objects beyond Neptune's orbit (Table 2). Its visible geometric albedo $p_V = 0.96^{+0.09}_{-0.04}$ (Sicardy et al. 2011) is the highest measured on any object beyond Neptune and matches that of Mimas and Rhea, mid-sized satellites of Saturn that are embedded in and impacted by the giant planet's dusty E-ring (Verbiscer et al. 2007). Eris's geometric albedo is much higher than that of Pluto and Haumea, the only other objects beyond Neptune that are larger than Makemake (Table 3). Its only known satellite, Dysnomia, is much darker ($p_V = 0.04$) than Eris and has a diameter of $\sim$700 km (Brown & Butler 2018). Eris has a low total amplitude ($\Delta m = 0.06$ mag) rotation curve with a period of 349.44 ± 2.4 hr (Holler et al. 2020). Multichord stellar occultation results (Sicardy et al. 2011) show that its shape is likely spherical, so the amplitude of its rotation curve is not expected to increase at higher phase angles as the amplitudes of the rotation curves of irregularly shaped asteroids (Gehrels 1956; Lu & Jewitt 2019) and Saturnian satellites do (Denk & Mottola 2019).

Methane is the most spectroscopically dominant molecule on Eris's surface (Brown et al. 2005b; Licandro et al. 2006a; Dumas et al. 2007; Merlin et al. 2009; Snodgrass et al. 2010; Alvarez-Candal et al. 2011; Hainaut et al. 2012). Although nitrogen ice has not been directly detected on Eris's surface, Merlin et al. (2009) and Alvarez-Candal et al. (2011) infer its presence owing to shifts in the positions of absorption bands of CH$_4$ that point to a dilution of nitrogen ice in methane ice. Furthermore, Alvarez-Candal et al. (2011) conclude that the surface composition of Eris is heterogeneous, with pure methane ice spatially segregated. Eris's $B - V$ and $V - R$ color indices are less red than those of Pluto (Table 2).

New Horizons LORRI observed Eris during three visits separated by 2 days in 2020 May at solar phase angle $\alpha = 24°.8$, acquiring 60 65 s images in each visit (Table 4). We combine low phase angle, ground-based observations of Eris in V from Rabinowitz et al. (2007), DeMeo et al. (2009), and Merlin et al. (2009) with high phase angle observations obtained by New Horizons LORRI (Table 4) to construct Eris's solar phase curve covering the range in α between $0°.16$ and $25°$ (Figures 3–5), and we discuss modeling the phase curve in Section 3.1. Eris will not undergo a node crossing and reach true opposition until 2074, and the smallest phase angle at which Eris has been observed is $\alpha = 0°.14$ (Duffard et al. 2008). Eris's color over the LORRI bandpass (350–850 nm) is closer to that of Charon than that of Pluto, the Sun, or Arrokoth (Table 2); therefore, we apply the Weaver et al. (2020) Charon color correction, CC $= -0.014$ mag, to transform the LORRI observations to Johnson V.

2.2. Dwarf Planet (136472) Makemake

Discovered in 2005 during a survey conducted by Palomar Observatory (Brown 2008), DP (136472) Makemake (2005 FY$_9$) is the third largest ($D \sim 1420$ km; Lim et al. 2010; Ortiz et al. 2012; Brown 2013) of the known objects beyond Neptune's orbit (Table 2). Its visible geometric albedo $p_V = 0.82 \pm 0.02$ (Hromakina et al. 2019) is second only to that of Eris and much higher than that of Pluto and Haumea, the only other DPs beyond Neptune (Table 3). It has a darker satellite with a diameter of $\sim$200 km (Parker et al. 2016). Makemake has a low-amplitude ($\Delta m = 0.032 \pm 0.005$ mag) rotation curve with a period of 22.8266 ± 0.0001 hr (Heinze & de Lahunta 2009; Hromakina et al. 2019). Makemake's near-infrared spectrum contains strong methane absorption bands, indicating that, like Pluto and Eris, methane plays a major role in its surface composition, although there is not as much nitrogen on Makemake's surface as seen on Pluto and Eris (Licandro et al. 2006b; Brown et al. 2007a, 2015; Tegler et al. 2007, 2008; Lorenzi et al. 2015; Perna et al. 2017; Holler et al. 2019). Makemake's visible color indices demonstrate that its surface is somewhat redder than that of Eris, but not as red as Pluto's surface (Table 2).

New Horizons LORRI observed Makemake in 2007 October at solar phase angle $\alpha = 8°$, about 7 months after the spacecraft flew past Jupiter (Stern et al. 2007), and once again during two visits on consecutive days in 2017 January at solar phase angle $\alpha = 32°$ (Table 5). The 2017 January observations were acquired during two epochs 17.5 hr, or three quarter rotations of Makemake, apart. While the average difference of 0.08 mag

Table 5
LORRI Observations of Dwarf Planet (136472) Makemake

Observation Mid-time	r (au)	Δ (au)	α (deg)	Exposure Time (s)	Total Images	LORRI Magnitude	V Magnitude at 1 au[a]
2007-10-06 00:50	52.020	52.048	8.391	9.967	5	17.526 ± 0.015	0.349
2007-10-06 15:50	52.020	52.051	8.397	9.967	5	17.518 ± 0.010	0.341
2017-01-28 08:52	52.475	69.718	32.023	9.967	30	18.501 ± 0.031	0.671
2017-01-28 09:50	52.475	69.718	32.023	9.967	30	18.661 ± 0.038	0.831
2017-01-29 02:21	52.475	69.722	32.027	9.967	30	18.486 ± 0.029	0.656
2017-01-29 03:19	52.475	69.722	32.027	9.967	30	18.493 ± 0.041	0.663
2007-10-06 08:20	52.020	52.050	8.394	9.967	10	17.522 ± 0.009	0.345[b]
2017-01-28 18:06	52.475	69.720	32.025	9.967	120	18.535 ± 0.017	0.705

Notes.
[a] Since Makemake's color over the LORRI bandpass (350–850 nm) is similar to that of Charon (Table 2), we apply the Weaver et al. (2020) Charon color correction, -0.014 mag, to transform LORRI magnitudes to the Johnson V magnitude of Makemake viewed at 1 au from the Sun and 1 au from LORRI.
[b] Entries below the horizontal line include the mean observational circumstances of all LORRI observations of Makemake in 2007 and 2017 and the corresponding magnitudes of the stacks of 10 and 120 LORRI images, respectively.

between these two epochs may suggest that the amplitude of Makemake's rotation curve at $\alpha = 32°$ is at least ~ 0.08 mag, the compounded uncertainties in the LORRI observations either exceed or match the 0.032 mag amplitude of the low phase angle, Earth-based rotation curve. Since multichord stellar occultations have confirmed Makemake's nearly spherical shape (Ortiz et al. 2012), any variation in reflectance with rotation may be due to heterogeneity in its surface scattering properties or varying contributions from its satellite. We combine low phase angle, ground-based observations of Makemake in V from Hromakina et al. (2019) with high phase angle observations obtained by New Horizons LORRI during two epochs (Table 5) to construct Makemake's solar phase curve from $\alpha = 0°\!.5$–$32°$ (Figures 3–5), and we discuss modeling this phase curve in Section 3.1. By combining observations acquired at two different epochs separated by 10 yr, we assume that Makemake's surface did not change from 2007 to 2017, despite the fact that the surface is rich in volatiles. Makemake does not reach true opposition until 2102, and the smallest phase angle at which Makemake has been observed is $\alpha = 0°\!.5$ (Hromakina et al. 2019). Makemake's color over the LORRI bandpass (350–850 nm) is similar to that of Charon (Table 2); therefore, we apply the Weaver et al. (2020) Charon color correction, $CC = -0.014$ mag, to transform the LORRI observations to Johnson V.

2.3. Dwarf Planet (136108) Haumea

With its unusually large, nonspherical shape and ring (Ortiz et al. 2017; Dunham et al. 2019), two satellites (Brown et al. 2005a), and rapid rotation period (Lellouch et al. 2010), DP (136108) Haumea (2003 EL$_{61}$) is one of the most intriguing objects in the solar system. Haumea was discovered in 2004 as part of the same survey that found Eris in 2005. After Pluto, Eris, and possibly Makemake, it is the third (or fourth) most massive known object beyond Neptune. With a surface composed almost entirely of crystalline water ice (Tegler et al. 2007; Pinilla-Alonso et al. 2009), Haumea is the third most reflective DP with a visible geometric albedo $p_V = 0.66 \pm 0.02$ (Dunham et al. 2019). Only DPs Eris and Makemake have higher visible geometric albedos. Haumea has the only collisional family (Brown et al. 2007a; Rabinowitz et al. 2008) known in the Kuiper Belt, and its rapid 3.9 hr rotation and high-amplitude rotation curve (Table 3) also

suggest that Haumea experienced a previous major collision (Brown et al. 2007b).

Along with Makemake, New Horizons LORRI also observed Haumea in 2007 October at solar phase angle $\alpha = 8°$. New Horizons obtained additional observations of Haumea during two visits on consecutive days in 2017 January at solar phase angle $\alpha = 39°$ and during two visits in 2020 May at $\alpha = 48°$. Table 6 summarizes the New Horizons LORRI observations of Haumea.

The Haumea system's Earth-based rotation curve (Lacerda et al. 2008; see Figure 1) has the highest amplitude in the V band (~ 0.3 mag; Table 3) of any of the DPs, primarily due to Haumea's nonspherical shape. Because the rotation period of Haumea is known to high accuracy (3.915341 ± 0.000005 hr; Lellouch et al. 2010), all LORRI observations can be phased on a rotation curve using the point of minimum reflectance from the Haumea system as 0 rotation phase and $0°$ longitude as defined by Lockwood et al. (2014) at JD 2454867.042. For each LORRI visit in Table 6 we calculate the subspacecraft longitude to determine the rotation phase at Haumea. Magnitudes for the 2007 New Horizons observations acquired at the smallest solar phase angle, $\alpha = 8°$, are measured relative to the mean magnitude of the Lacerda et al. (2008) rotation curve, using the Haumea system phase coefficient ($\beta = 0.110 \pm 0.014$; Rabinowitz et al. 2007) to correct to H_V in 2007. The 2007 LORRI observations fall on the Earth-based rotation curve acquired at phase angles $\alpha < 1°\!.1$, suggesting that the total amplitude of the Haumea system rotation curve does not increase significantly at $\alpha = 8°$. Magnitudes for the 2017 and 2020 LORRI observations are measured relative to the median magnitude at each epoch, and these observations do not fall on the Lacerda et al. (2008) rotation curve. Because the 2020 LORRI observations sample a full rotation, they suggest that the total amplitude of the Haumea system rotation curve increases to 0.6 ± 0.2 mag at $\alpha = 48°$. A two-term Fourier fit to the 2020 LORRI data set (dashed line in Figure 1) has a total amplitude 0.6 ± 0.2 mag, twice that of the Earth-based rotation curve (solid line in Figure 1), although the uncertainty in this amplitude is high, due to the high uncertainties in the reflectance measured at each visit. The 2017 LORRI observations, on the other hand, only sampled half a rotation, so it is not possible to fit a curve to those data, and the median magnitude of four points in half a rotation may not represent

Table 6
LORRI Observations of the Dwarf Planet (136108) Haumea System

Observation Mid-time	r (au)	Δ (au)	Sub-s/c Lat (deg)	Sub-s/c Lon (deg)[a]	α (deg)	Exposure Time (s)	Total Images	LORRI Magnitude	V Magnitude at 1 au[b]
2007-10-06 1:50	51.141	48.759	2.1	89.3	8.299	9.967	5	17.660 ± 0.086	0.676
2007-10-06 16:50	51.141	48.760	2.1	28.4	8.307	9.967	5	17.869 ± 0.098	0.885
2017-01-29 04:16	50.591	58.638	25.1	2.2	39.370	9.967	30	19.488 ± 0.147	2.127
2017-01-29 04:45	50.591	58.638	25.1	45.8	39.370	9.967	30	18.835 ± 0.089	1.474
2017-01-30 00:49	50.591	58.641	25.1	91.3	39.376	9.967	30	18.738 ± 0.083	1.378
2017-01-30 01:18	50.591	58.641	25.1	136.8	39.377	9.967	30	18.679 ± 0.079	1.318
2020-05-29 00:54	50.329	63.087	30.5	269.0	47.808	64.967	20	19.149 ± 0.157	1.640
2020-05-29 01:53	50.329	63.087	30.5	355.9	47.809	64.967	20	19.405 ± 0.200	1.896
2020-05-31 01:51	50.329	63.094	30.5	89.7	47.822	64.967	20	18.814 ± 0.126	1.305
2020-05-31 02:49	50.329	63.094	30.5	178.6	47.822	64.967	20	19.399 ± 0.184	1.890

Notes.
[a] Dividing the subspacecraft longitude by 360° yields the rotational phase in Figure 1.
[b] Since Haumea's color indices over the LORRI bandpass (350–850 nm) are similar to those of the Sun (Table 2), we apply the Weaver et al. (2020) solar color correction, 0.0 mag, to transform LORRI magnitudes to the Johnson V magnitude of Haumea viewed at 1 au from the Sun and 1 au from LORRI.
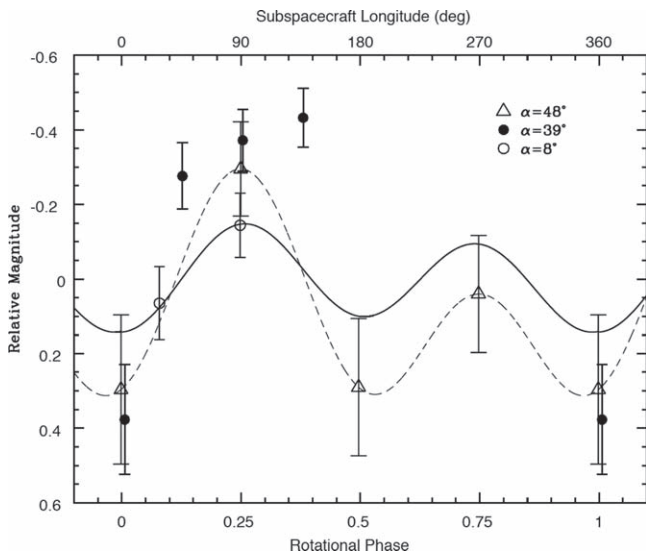
Figure 1. Earth-based rotation curve of the Haumea system (solid line) from Lacerda et al. (2008) and New Horizons LORRI observations acquired at three different epochs in 2007 October (open circles), 2017 January (filled circles), and 2020 May (triangles) (Table 6). All observations are phased to 0 rotation phase and 0° longitude at JD 2454867.042 as defined by Lockwood et al. (2014). See text for further details on the placement of LORRI observations on these rotation curves. The New Horizons observations acquired at $\alpha = 8°$ fall on the Earth-based light curve with amplitude 0.29 mag (Table 3), while those acquired at $\alpha = 48°$ demonstrate that the amplitude of Haumea's light curve increases at higher phase angles, as expected for a nonspherical body. The dashed line is a two-term Fourier fit to the 2020 LORRI observations with total amplitude 0.6 ± 0.2 mag. Note that the secondary peak at subspacecraft longitude 270° (rotational phase 0.75) in the 2020 LORRI rotation curve coincides with the location of a dark red spot on Haumea identified by Lacerda et al. (2008). Error bars represent one standard deviation from the mean reflectance in all images at each visit.

the true median of a full rotation. These observations of the Haumea system rotation curves at high phase angles attainable only by spacecraft may place constraints on the shape of Haumea; however, the degeneracy between the DP's shape and the variation in reflectance on its surface, with both latitude and longitude, remains.

We combine low phase angle, ground-based observations of the Haumea system in V from Rabinowitz et al. (2006) with high phase angle observations obtained by New Horizons LORRI during three epochs (Table 6) to construct its solar

phase curve from $\alpha = 0°.5$ to $48°$ (Figures 3–5). Because the projected area of Haumea changes for each apparition seen from New Horizons, placing the LORRI observations on the Haumea system solar phase curve is not as straightforward as it is for the other, spherical DPs, which do not have changing projected areas. The Haumea system H_V magnitude changes with changing viewing geometry, both from Earth, as shown by Ortiz et al. (2017), and from New Horizons. We normalize the Haumea system solar phase curve to the visible geometric albedo of the Haumea system in 2017, when New Horizons observed the system only 8 days after a stellar occultation on January 21 (Ortiz et al. 2017) measured the size of Haumea and discovered its ring. Using the stellar occultation chords, Dunham et al. (2019) determined the geometric albedo of Haumea, $p_V = 0.66 \pm 0.02$; however, we need to use the combined geometric albedo of Haumea and its satellites and ring. Ortiz et al. (2017) found that Haumea's ring is 70 km wide and assumed that the ring has $I/F \simeq 0.09$, based on the reflectivity of Chariklo's ring (Braga-Ribas et al. 2014). Ragozzine & Brown (2009) estimated that Haumea's largest moon, Hi'iaka, is 10 times fainter than Haumea and that the smaller moon, Namaka, is 3.7 times fainter than Hi'iaka, while Brown et al. (2006) found that Hi'iaka and Namaka are 5% and 1.5%, respectively, as reflective as Haumea. Therefore, according to Ortiz et al. (2017), the satellites and ring contribute 11% and 2.5% to the total flux of the Haumea system viewed from Earth in 2017, so the geometric albedo of the Haumea system is then $p_V = 0.75 \pm 0.02$. In order to normalize each data set to the geometric albedo viewed from Earth in 2017, we must first determine the H_V magnitude of the Haumea system that corresponds to a geometric albedo of $p_V = 0.75$ by using

$$p_V = \frac{10^{0.4(V_\odot - H_V)}}{A/\pi}, \qquad (2)$$

where $V_\odot$ is the V magnitude of the Sun, -26.74; H_V is the instantaneous absolute magnitude of Haumea from the rotationally averaged absolute magnitude (in 2007), or the median magnitude at each epoch (in 2017 and 2020); and A is the projected area of Haumea seen from LORRI in au^2. We use the equations provided by Dunham et al. (2019) to calculate the apparent semimajor and semiminor axes of Haumea seen from

Table 7
LORRI Observations of Large Classical KBO (50000) Quaoar

Observation Mid-time	r (au)	Δ (au)	α (deg)	Exposure Time (s)	Total Images	LORRI Magnitude	V Magnitude at 1 au[a]
2016-07-13 02:02	42.952	13.867	51.182	9.967	24	17.918 ± 0.048	4.110
2016-07-13 04:10	42.952	13.867	51.185	9.967	24	18.260 ± 0.063	4.452
2016-07-14 00:08	42.952	13.864	51.210	9.967	24	18.052 ± 0.054	4.245
2016-07-14 02:20	42.952	13.863	51.213	9.967	24	17.889 ± 0.048	4.082
2017-09-18 18:03	42.914	12.471	65.762	9.967	40	17.919 ± 0.038	4.343
2017-09-18 20:11	42.914	12.471	65.765	9.967	40	18.138 ± 0.046	4.562
2017-09-19 16:11	42.914	12.469	65.796	9.967	40	18.102 ± 0.043	4.527
2017-09-19 18:19	42.914	12.468	65.799	9.967	40	18.000 ± 0.039	4.425
2019-01-06 00:07	42.871	11.848	84.241	29.967	26	18.250 ± 0.061	4.788
2019-01-06 02:20	42.871	11.848	84.245	29.967	26	18.423 ± 0.070	4.961
2019-01-06 04:33	42.871	11.848	84.248	29.967	26	18.281 ± 0.065	4.819
2019-01-07 00:07	42.871	11.848	84.241	29.967	26	18.292 ± 0.064	4.830
2019-01-07 02:20	42.871	11.848	84.285	29.967	26	18.290 ± 0.064	4.828
2019-01-07 04:33	42.871	11.848	84.289	29.967	26	18.360 ± 0.066	4.898
2019-09-01 11:41	42.849	11.946	93.807	64.967	10	18.496 ± 0.081	5.017
2019-09-01 12:00	42.849	11.946	93.808	29.967	20	18.420 ± 0.111	4.941
2019-09-01 13:54	42.849	11.946	93.811	64.967	10	18.609 ± 0.094	5.130
2019-09-01 14:13	42.849	11.946	93.812	29.967	20	18.479 ± 0.120	5.000
2019-09-01 16:06	42.849	11.946	93.815	64.967	10	18.622 ± 0.096	5.143
2019-09-01 16:25	42.849	11.946	93.815	29.967	20	18.607 ± 0.135	5.128
2019-09-01 18:19	42.849	11.946	93.818	64.967	10	18.523 ± 0.087	5.044
2019-09-01 18:38	42.849	11.946	93.819	29.967	20	18.439 ± 0.114	4.960

Note.

[a] Since Quaoar's color over the LORRI bandpass (350–850 nm) is similar to that of other classical KBOs (Table 2), we apply the Weaver et al. (2020) color correction for CCKBO Arrokoth, +0.067 mag, to transform LORRI magnitudes to the Johnson V magnitude of Quaoar viewed at 1 au from the Sun and 1 au from LORRI.

LORRI and use these to determine the projected area A for each epoch. Inserting the distance-corrected median magnitude (for 2017 and 2020) and rotation-corrected magnitude (for 2007) and projected area A into Equation (2) provides the reflectance (I/F) at a given phase angle that can be placed on the solar phase curve, following normalization to the geometric albedo $p_V = 0.75$.

We combine low phase angle, Earth-based observations of Haumea in V from Rabinowitz et al. (2007) with high phase angle observations obtained by New Horizons LORRI during four epochs (Table 6) to construct Haumea's solar phase curve from $\alpha = 0°.51$ to $48°$ (Figures 3–5). Haumea's colors over the LORRI bandpass (350–850 nm) approximate those of the Sun (Table 2); therefore, we apply the Weaver et al. (2020) solar color correction, $CC = 0.0$ mag, to transform the LORRI observations to Johnson V.

2.4. Large Classical KBO (50000) Quaoar

Classical KBO (50000) Quaoar (2002 LM$_{60}$) was discovered in 2002, and observations in 2004 by the HST's Advanced Camera for Surveys (ACS) estimated its diameter at 1260 ± 190 (Brown & Trujillo 2004). Stellar occultations (Person et al. 2011; Sallum et al. 2011; Braga-Ribas et al. 2013; Pasachoff et al. 2013; Davis et al. 2014; Kretlow 2019) subsequently measured Quaoar's mean diameter, 1110 ± 5 km, and determined the KBO's visible geometric albedo, $p_V = 0.109 \pm 0.007$ (Braga-Ribas et al. 2013). Quaoar's surface composition contains crystalline water ice (Jewitt & Luu 2004; Barucci et al. 2015) with small amounts (∼5%) of methane (Schaller & Brown 2007) and ethane (Dalle Ore et al. 2009). Quaoar's one known satellite, Weywot (Brown & Suer 2007),

is ∼170 km in diameter and darker than Quaoar itself (Kretlow 2019).

New Horizons observed Quaoar during four visits in 2016, four visits in 2017, and 20 visits in 2019 at solar phase angles $\alpha = 51°$, $66°$, $84°$, and $94°$. Table 7 summarizes the LORRI Quaoar observations and photometry. LORRI acquired multiple images during each visit; however, only the visits in 2019 January and September at phase angles $\alpha = 84°$ and $94°$ provided a sufficient number of observations over Quaoar's 8.84 hr rotation period (Rabinowitz et al. 2007; Thirouin 2013) to evaluate its rotation curve at these high phase angles (Figure 2). At small phase angles, Quaoar has a low-amplitude rotation curve, 0.112 ± 0.011 mag (Thirouin 2013; see Table 3). Placing the New Horizons LORRI images at $\alpha = 51°$, $66°$, $84°$, and $94°$ on Quaoar's rotation curve demonstrates that, within the uncertainties, the amplitude of Quaoar's rotation curve does not increase with increasing phase angle. Whether the observed variation in Quaoar's reflectance with rotation phase is due to surface albedo variations or the KBO's shape, or both, cannot be established from this sparse data set.

We combine low phase angle, Earth-based observations of Quaoar in V from Rabinowitz et al. (2007) with high phase angle observations obtained by New Horizons LORRI during four epochs (Table 7) to construct Quaoar's solar phase curve from $\alpha = 0°.17$ to $94°$ (Figures 3–5). Quaoar's color over the LORRI bandpass (350–850 nm) is similar to that of other classical KBOs (Hainaut et al. 2012; see Table 2); therefore, we apply the Weaver et al. (2020) color correction for CCKBO Arrokoth, $CC = +0.067$ mag, to transform the LORRI observations to Johnson V. Arrokoth's $V - I$ color is 1.35 (Benecchi et al. 2019).
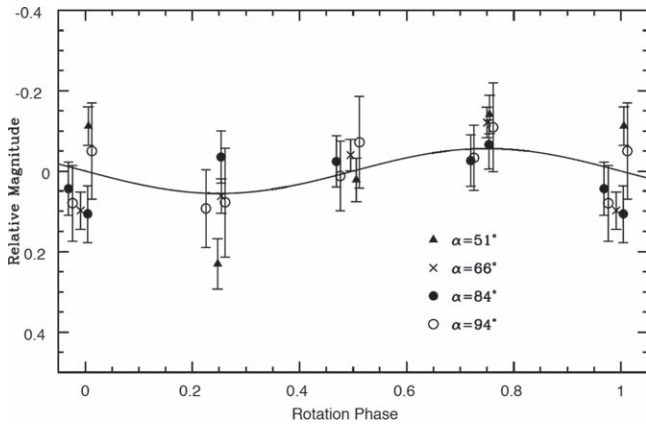
Figure 2. Earth-based *V*-band rotation curve of Quaoar from Thirouin ([2013](#)) (solid line) with total amplitude 0.112 ± 0.011 (Table [3](#)). New Horizons LORRI observations at $\alpha = 51°$ (triangles), $\alpha = 66°$ (crosses), $\alpha = 84°$ (filled circles), and $94°$ (open circles) fall on the Earth-based rotation curve, demonstrating that the amplitude of Quaoar's rotation curve does not increase at higher solar phase angles. Error bars represent one standard deviation from the mean reflectance in all images at each visit. Rotation phase 0 is JD 2458400.95.

2.5. Large Classical KBO (307261) 2002 MS₄

(307261) 2002 MS₄ (hereafter MS₄) was discovered by Trujillo & Brown ([2003](#)) (MPEC 2002-27) using the 1.2 m Schmidt telescope on Mt. Palomar. Since its discovery, MS₄ has been moving through a dense star field, making Earth-based observations challenging; however, that dense star field increases the likelihood that MS₄ will occult one of those background stars. A multichord stellar occultation by MS₄ on 2020 August 8 measured its shape, $(808 \pm 10.8) \times (748 \pm 15.3)$ km, and geometric albedo $p_V = 0.076$ (Rommel et al. [2020](#)). Thirouin ([2013](#)) found that MS₄ has a low-amplitude, single-peaked rotation light curve (0.05 ± 0.01 mag) with a period of 7.33 hr (Table [3](#)). The $B - V$ and $V - R$ colors of MS₄ are similar to those of Haumea (Table [2](#)), although Haumea's visible geometric albedo is considerably higher than MS₄'s.

Table [8](#) summarizes the Earth-based observations of 2002 MS₄ from Peng ([2022](#)), acquired by the MegaPrime/MegaCam instrument at the Canada–France–Hawaii Telescope (CFHT) between phase angles $\alpha = 0°.037$ and $1°.2$ and corrected for variation in reflectance due to rotation. We use the transformations provided by Betoule et al. ([2013](#)) and the color of MS₄, $g' - r' = 0.499 \pm 0.023$ (Peng [2022](#)), to correct the Mega-Prime/MegaCam r_M filter data to the Johnson *V* magnitude of MS₄ with the color correction $V - r_M = +0.191$ mag. We combine the low phase angle CFHT observations of MS₄ (Table [8](#)) with high phase angle observations obtained by New Horizons LORRI during three epochs (Table [9](#)) to construct 2002 MS₄'s solar phase curve from $\alpha = 0°.367$ to $76°$ (Figures [3–5](#)). The color of MS₄ over the LORRI bandpass (350–850 nm) is similar to that of the Sun (Table [2](#)); therefore, we apply the Weaver et al. ([2020](#)) solar color correction, $CC = 0.0$ mag, to transform the LORRI observations to Johnson *V*.

2.6. Large Plutino (28978) Ixion

(28978) Ixion (2001 KX₇₆) was discovered on 2001 May 22 by the Deep Ecliptic Survey (MPEC 2001-N01). Ixion is classified a Plutino since it is in a 3:2 mean-motion resonance
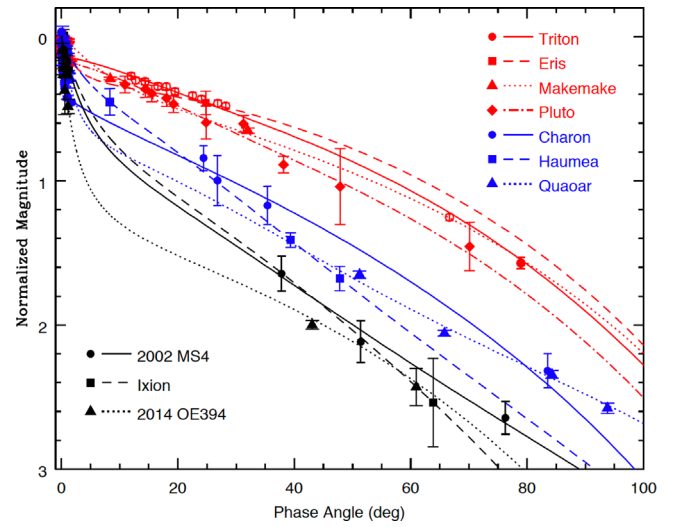

Figure 3. Solar phase curves from the Earth-based and New Horizons LORRI observations in Tables [4–10](#) and [12–13](#) for all DPs, large KBOs, and satellites observed by New Horizons. All data at phase angles $\alpha < 2°$ are from Earth-based observations summarized in Tables [3](#) and [11](#), and all data at phase angles $\alpha > 2°$ are from New Horizons LORRI (filled circles) and Voyager 2 (open circles). See Section [2](#) for descriptions of the data sets for each object and Figure [4](#) for details of the near-opposition portion of each solar phase curve. All phase curves are normalized to 0 mag at opposition ($\alpha = 0°$) to enable direct comparison of their shapes. All lines are fits to the Hapke ([2012b](#)) photometric model using parameters given in Table [14](#) for the DPs, large KBOs, Triton, and Charon. Error bars represent one standard deviation from the mean reflectance in all images at each visit.

with Neptune. A multichord stellar occultation on 2020 October 13 measured Ixion's shape, 756.9×684.9 km, which is consistent with a mean diameter 709.6 ± 0.2 km for a spherical body (Levine et al. [2021](#)). Using the absolute magnitude $H_V = 3.774 \pm 0.021$ measured by Alvarez-Candal et al. ([2016](#)) gives a geometric albedo $p_V = 0.108 \pm 0.002$. Galiazzo et al. ([2016](#)) found that Ixion has a rotation period of 12.4 ± 0.3 hr with a low-amplitude (<0.1 mag) rotation curve. Prior to that observation, Rousselot & Petit ([2010](#)) measured Ixion's rotation curve with a period 15.9 ± 0.5 hr and amplitude 0.06 ± 0.03 mag (Table [3](#)). Ortiz et al. ([2003](#)) observed Ixion in 2001 and were not able to derive a rotation period but established that the amplitude of its rotation curve was <0.15 mag with no filter. Sheppard & Jewitt ([2003](#)) measured a single-peaked rotation curve with amplitude <0.05 mag in the *R* band.

Ixion's $B - V$ and $V - R$ color indices and visible geometric albedo are similar to those of Quaoar, although Quaoar is the larger of the two KBOs (Table [2](#)). While the presence of crystalline water ice on Quaoar's surface has been confirmed, water ice has not been directly detected on Ixion (Licandro et al. [2002](#)), although Barkume et al. ([2008](#)) report a possible detection of water ice on Ixion's surface. Boehnhardt et al. ([2004](#)) modeled Ixion's near-infrared spectrum with an areal mixture of 65% amorphous carbon, 13% Titan tholin, 20% ice tholin, and 2% water ice.

New Horizons observed Ixion during two visits on 2016 July 13 and 14; however, the visit on July 13 is contaminated with a background source, leaving only the July 14 visit usable for photometric analysis. We combine low phase angle, Earth-based observations of Ixion in *V* from Doressoundiram et al. ([2002](#)) and DeMeo et al. ([2009](#)) and in *R* converted to *V* from Boehnhardt et al. ([2004](#)) with high phase angle observation
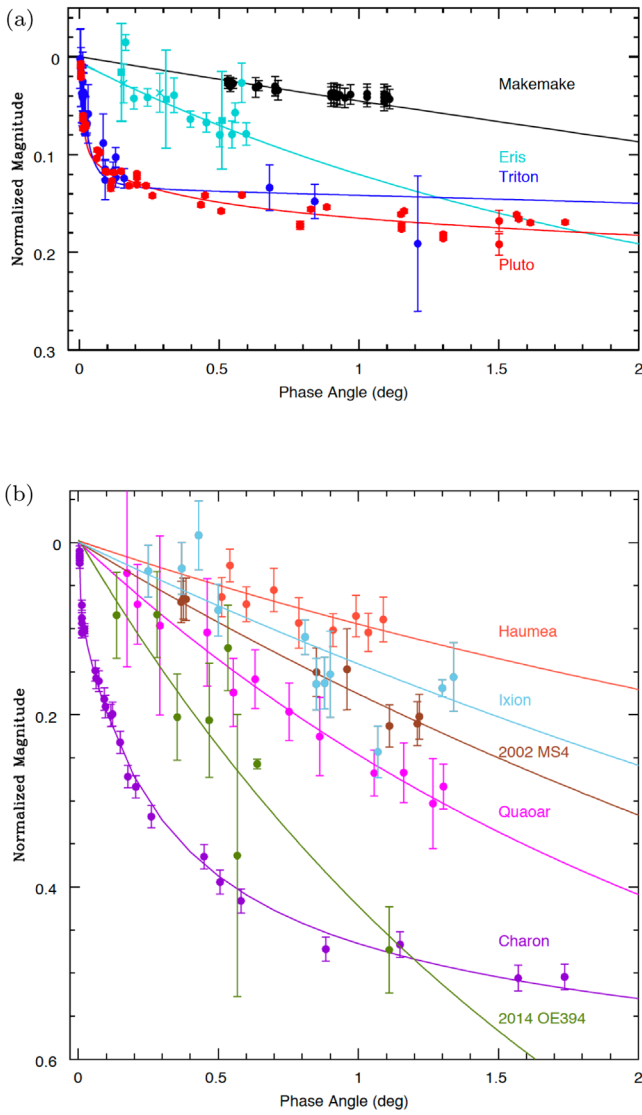
Figure 4. Near-opposition portions of solar phase curves of satellites and DPs with (a) volatile-rich and (b) water ice-rich and nonvolatile surfaces, although the surface compositions of 2002 MS$_4$ and 2014 OE$_{394}$ have not yet been determined. The scatter in the low phase angle points for 2014 OE$_{394}$ and Ixion is due to the variation in their reflectance with rotation (i.e., rotation curve). The Makemake, Eris, Pluto, Triton, Haumea, Charon, 2002 MS$_4$, and Quaoar observations have all been corrected for variation in reflectance due to their rotation curves. Error bars represent one standard deviation from the mean reflectance in all images at each phase angle. (a) DPs and satellites with hypervolatile-rich surfaces. (b) DPs and large KBOs with H$_2$O-rich (Haumea, Quaoar, and Charon), volatile-poor (Ixion), and undetermined (2002 MS$_4$ and 2014 OE$_{394}$) surface compositions.

obtained by New Horizons LORRI in 2016 July (Table 10) to construct Ixion's solar phase curve from $\alpha = 0°.03$ to 64° (Figures 3–5). The uncertainties in both measurements of Ixion's rotation period, 15.9 ± 0.5 hr and 12.4 ± 0.3 hr, are too large to place observations acquired by LORRI in 2016 and Rabinowitz et al. (2007) in 2003 on its rotation curve; therefore, we do not apply any correction for the variation in reflectance with rotation phase to the LORRI or Earth-based observations. Since the amplitude of Ixion's rotation curve is small, the errors introduced by omitting these corrections for variation in reflectance due to rotation are similarly small. The color of Ixion over the LORRI bandpass (350–850 nm) is similar to that of Quaoar and CCKBOs (Table 2); therefore, as
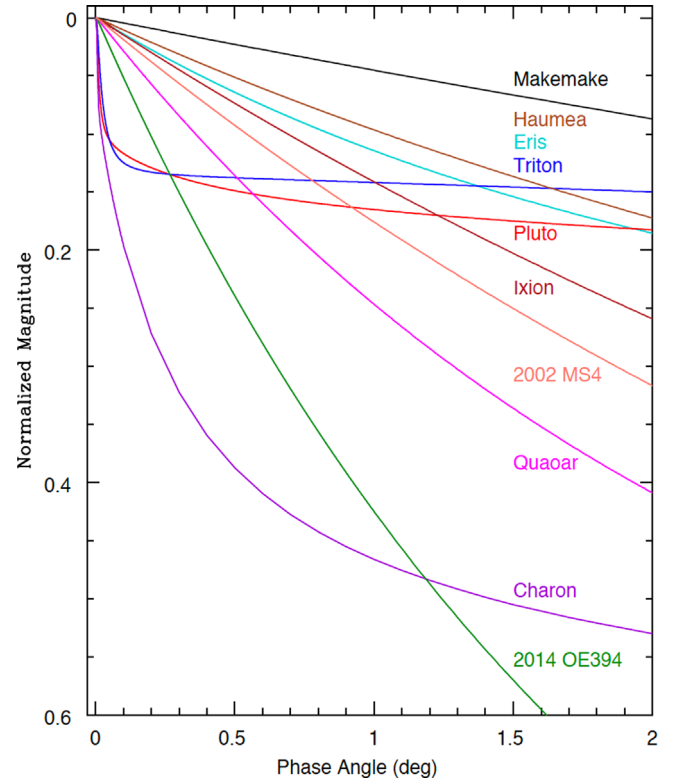
Figure 5. Near-opposition portions of all solar phase curves in Figure 3 for each DP, large KBO, and satellites. All phase curves are normalized to 0 mag at opposition ($\alpha = 0°$) to enable direct comparison of their shapes at phase angles $\alpha < 2°$.

we did for Quaoar, we apply the Weaver et al. (2020) Arrokoth color correction, CC $= +0.067$ mag, to transform the LORRI observation to Johnson V.

2.7. Large Cold Classical KBO (556416) 2014 OE$_{394}$

CCKBO 2014 OE$_{394}$ (hereafter OE$_{394}$) was discovered in 2014 July by the Panoramic Survey Telescope and Rapid Response System (Pan-STARRS; MPEC 2016-O95). Because no radiometric or thermal measurements of OE$_{394}$ exist, nor have there been stellar occultations from which to measure its size and albedo, we adopt the visible geometric albedo of the average CCKBO, $p_V = 0.15^{+0.08}_{-0.06}$ (Lacerda et al. 2014), for OE$_{394}$. For a KBO with $H_V = 4.8$, a visible geometric albedo $p_V = 0.15^{+0.08}_{-0.06}$ corresponds to a mean diameter in the range 304–486 km (Table 2), making OE$_{394}$ a large KBO, possibly a DP candidate.

Table 11 summarizes all Earth-based observations of OE$_{394}$ acquired in 2011–2015 from Pan-STARRS at solar phase angles in the range $\alpha = 0°.137$–$1°.215$ and in 2020 from the Apache Point Observatory (APO) Astrophysical Research Consortium's 3.5 m telescope at phase angles $\alpha = 0°.46$ and $0°.64$. While these observations provide contributions to OE$_{394}$'s solar phase curve at small phase angles, the sampling is not sufficient to characterize its rotation curve in the low phase angle regime. We average data from each night's observations to provide a point on OE$_{394}$'s solar phase curve at the phase angle available on each night. The Gaia Data Release 2 (GDR2) archive (Gaia Collaboration et al. 2016, 2018) provides absolute photometry for the APO observations, and we use the transformations $G - r'$ provided

Table 8
Earth-based Observations of Large Classical KBO (307261) 2002 MS$_4$

Observation Mid-time	r (au)	Δ (au)	α (deg)	Instrument[a]	Filter[b]	Total Images	Magnitude	V Magnitude at 1 au[c]
2013-07-04 11:19	46.996	46.024	0.367	MegaPrime/MegaCam	r_M	8	20.121 ± 0.007	3.692
2013-07-05 11:58	46.996	46.026	0.376	MegaPrime/MegaCam	r_M	12	20.206 ± 0.006	3.688
2013-07-06 11:19	46.996	46.028	0.385	MegaPrime/MegaCam	r_M	4	20.180 ± 0.009	3.689
2013-08-08 08:07	46.990	46.250	0.851	MegaPrime/MegaCam	r_M	3	20.308 ± 0.016	3.774
2013-08-31 08:25	46.986	47.570	1.111	MegaPrime/MegaCam	r_M	4	20.364 ± 0.008	3.771
2013-11-06 04:40	46.974	46.544	0.960	MegaPrime/MegaCam	r_M	2	20.284 ± 0.041	3.836
2014-09-19 05:20	46.920	46.751	1.211	MegaPrime/MegaCam	r_M	2	20.305 ± 0.011	3.834
2014-09-22 05:17	46.919	46.800	1.218	MegaPrime/MegaCam	r_M	2	20.288 ± 0.012	3.825

Notes.
[a] All observations from Peng (2022) were acquired by MegaPrime/MegaCam, the wide-field optical imaging facility at the CFHT.
[b] The MegaPrime/MegaCam r_M filter passband nearly matches that of the SDSS r' filter (Regnault et al. 2009).
[c] Color corrections for these Earth-based observations use the color of MS$_4$ provided by Peng (2022), $g' - r' = 0.499 \pm 0.023$. We use the transformations provided by Betoule et al. (2013) to derive the color correction $V - r_M = +0.191$ mag to correct the MegaPrime/MegaCam r_M filter data to Johnson V magnitude of MS$_4$ viewed at 1 au from the Sun and 1 au from Earth.

Table 9
LORRI Observations of Large Classical KBO (307261) 2002 MS$_4$

Observation Mid-time	r (au)	Δ (au)	α (deg)	Exposure Time (s)	Total Images	LORRI Magnitude	V Magnitude at 1 au[a]
2016-07-13 15:03	46.799	15.339	37.777	9.967	30	19.725 ± 0.199	5.445
2016-07-14 07:33	46.798	15.336	37.794	9.967	30	19.369 ± 0.142	5.089
2017-10-31 00:02	46.706	13.256	51.392	9.967	25	19.802 ± 0.237	5.843
2017-11-01 00:02	46.706	13.252	51.424	9.967	25	19.758 ± 0.331	5.800
2017-11-02 00:02	46.706	13.249	51.457	9.967	25	19.532 ± 0.189	5.574
2019-09-01 20:37	46.570	12.006	76.207	29.967	50	20.024 ± 0.201	6.314
2019-09-02 21:53	46.569	12.005	76.249	29.967	50	19.954 ± 0.186	6.198
2019-09-04 15:48	46.569	12.005	76.317	29.967	50	20.027 ± 0.203	6.290

Note.
[a] Since the color of 2002 MS$_4$ over the LORRI bandpass is similar to that of the Sun (Table 2), we apply the Weaver et al. (2020) solar color correction, 0 mag, to transform LORRI magnitudes to Johnson V magnitude of 2002 MS$_4$ viewed at 1 au from the Sun and 1 au from LORRI.

Table 10
LORRI Observation of Large Plutino (28978) Ixion

Observation Mid-time	r (au)	Δ (au)	α (deg)	Exposure Time (s)	Total Images	LORRI Magnitude	V Magnitude at 1 au[a]
2016-07-14 06:32	39.932	15.108	63.854	9.967	30	20.246 ± 0.306	6.410

Note.
[a] Since the color of Ixion over the LORRI bandpass is similar to that of Quaoar and CCKBOs (Table 2), we apply the Weaver et al. (2020) Arrokoth color correction, +0.067 mag, to transform LORRI magnitudes to the Johnson V magnitude of Ixion viewed at 1 au from the Sun and 1 au from LORRI.

by Busso et al. (2018) to measure OE$_{394}$'s magnitude on the Sloan Digital Sky Survey (SDSS) photometric system (Fukugita et al. 1996) in the r' filter. We use the transformations provided by Tonry et al. (2012) to derive the color correction $V - w_{P1} = +0.243$ mag to correct the Pan-STARRS1 w_{P1} filter data to Johnson V, and the transformations from Kostov & Bonev (2018) to derive the color corrections $V - g_{P1} = -0.405$, $V - r_{P1} = +0.456$, $V - i_{P1} = +0.95$, and $V - r' = +0.291$ transform Pan-STARRS1 g_{P1}, r_{P1}, i_{P1}, and SDSS r' filter data, respectively, to Johnson V. Future Earth-based observations of OE$_{394}$ acquired at a high cadence (sampling several times over the rotation period) are needed to provide additional near-opposition photometry, measure the

rotation period, and contribute to the determination of OE$_{394}$'s rotation pole and shape.

New Horizons observed OE$_{394}$ once each day for three consecutive days in 2017 September and again in 2018 August; Table 12 summarizes the observations from these six visits. However, the 24 hr observing cadence over 3 days is too sparse to construct rotation curves for OE$_{394}$ at $\alpha = 43°$ and 61°. The uncertainties in the individual observations at $\alpha = 43°$ are sufficiently small (0.03–0.1 mag) to place a lower limit, 0.74 ± 0.10 mag, on the amplitude of OE$_{394}$'s rotation curve at $\alpha = 41°$, since the highest and lowest magnitudes differ by this quantity. However, the larger uncertainties in the LORRI observations at $\alpha = 61°$ (0.21–0.24 mag) and the smaller

Table 11
Earth-based Observations of Large Cold Classical KBO (556416) 2014 OE$_{394}$

Observation Mid-time	r (au)	Δ (au)	α (deg)	Instrument[a]	Filter[b]	Total Images	Magnitude	V Magnitude at 1 au[c]
2011-08-04 08:39	44.592	43.679	0.568	Pan-STARRS1	r_{P1}	2	21.401 ± 0.071	5.244
2011-08-04 09:09	44.592	43.679	0.568	Pan-STARRS1	g_{P1}	2	21.549 ± 0.071	4.696
2012-06-14 11:19	44.684	43.754	0.535	Pan-STARRS1	w_{P1}	4	21.050 ± 0.050	4.837
2013-06-18 12:34	44.793	43.845	0.480	Pan-STARRS1	w_{P1}	4	21.200 ± 0.050	4.977
2014-07-28 09:06	44.913	43.932	0.354	Pan-STARRS1	w_{P1}	4	21.151 ± 0.050	4.918
2014-09-19 06:03	44.928	44.530	1.185	Pan-STARRS1	w_{P1}	4	21.576 ± 0.050	5.313
2014-09-23 06:15	44.929	44.596	1.215	Pan-STARRS1	w_{P1}	3	21.700 ± 0.058	5.434
2015-05-19 13:02	45.000	44.392	1.034	Pan-STARRS1	w_{P1}	4	21.225 ± 0.050	4.965
2015-05-21 13:20	45.001	44.365	1.008	Pan-STARRS1	w_{P1}	4	21.299 ± 0.050	5.040
2015-07-07 10:36	45.015	44.003	0.137	Pan-STARRS1	i_{P1}	4	20.850 ± 0.050	4.799
2015-07-26 10:07	45.020	44.027	0.282	Pan-STARRS1	i_{P1}	4	20.751 ± 0.050	4.798
2020-06-27 09:00	45.565	44.616	0.465	ARCTIC	SDSS r'	8	21.278 ± 0.021	4.910
2020-08-19 05:17	45.580	44.703	0.639	ARCTIC	SDSS r'	25	21.142 ± 0.003	4.917

Notes.
[a] Pan-STARRS1 is the Panoramic Survey Telescope and Rapid Response System Telescope #1 (Chambers et al. 2016). ARCTIC is the Astrophysical Research Consortium (ARC) Telescope Imaging Camera on the Apache Point Observatory's ARC 3.5 m telescope.
[b] The Pan-STARRS1 w_{P1} filter has a wide passband, approximating that of the combined g_{P1}, r_{P1}, and i_{P1} filter passbands. ARCTIC uses the SDSS filters (Fukugita et al. 1996).
[c] All color corrections for these Earth-based observations adopt the colors of CCKBO (486958) Arrokoth provided by Thirouin & Sheppard (2019). We use the transformations provided by Tonry et al. (2012) to derive the color correction $V - w_{P1} = +0.243$ mag to correct the Pan-STARRS1 w_{P1} filter data to Johnson V, and the transformations from Kostov & Bonev (2018) to derive the color corrections $V - g_{P1} = -0.405$, $V - r_{P1} = +0.456$, $V - i_{P1} = +0.95$, and $V - r' = +0.291$ transform Pan-STARRS g_{P1}, r_{P1}, i_{P1}, and SDSS r' filter data, respectively, to the Johnson V magnitude of OE$_{394}$ viewed at 1 au from the Sun and 1 au from Earth.

Table 12
LORRI Observations of Large Cold Classical KBO (556416) 2014 OE$_{394}$

Observation Mid-time	r (au)	Δ (au)	α (deg)	Exposure Time (s)	Total Images	LORRI Magnitude	V Magnitude at 1 au[a]
2017-09-19 00:02	45.258	8.508	43.038	9.967	25	19.236 ± 0.030	6.376
2017-09-20 00:02	45.258	8.504	43.084	9.967	25	19.307 ± 0.027	6.448
2017-09-21 00:02	45.259	8.500	43.130	9.967	25	19.976 ± 0.097	7.118
2018-08-20 17:07	45.360	7.569	60.877	29.967	26	19.865 ± 0.209	7.012
2018-08-21 17:07	45.361	7.568	60.936	29.967	26	19.923 ± 0.226	7.095
2018-08-22 17:07	45.361	7.567	60.995	29.967	26	19.876 ± 0.236	7.127

Note.
[a] Since we assume that OE$_{394}$'s color over the LORRI bandpass (350–850 nm) is similar to that of other CCKBOs (Table 2), we apply the Weaver et al. (2020) color correction for CCKBO Arrokoth, +0.067 mag, to transform LORRI magnitudes to the Johnson V magnitude of OE$_{394}$ viewed at 1 au from the Sun and 1 au from LORRI.

(0.027 mag) difference between the highest and lowest fluxes preclude the production of a rotation curve at $\alpha = 61°$. These LORRI observations provide no evidence of a high-amplitude rotation curve at $\alpha = 61°$.

We combine low phase angle Pan-STARRS and APO observations of OE$_{394}$ (Table 11) with high phase angle observations obtained by New Horizons LORRI at $\alpha = 43°$ and 61° (Table 12) to construct OE$_{394}$'s solar phase curve from $\alpha = 0°.14$ to 61° (Figures 3–5). Since the sampling is not sufficient to construct rotation curves at low or high phase angles, we do not apply any corrections for variation in reflectance due to rotation phase when constructing the solar phase curve for OE$_{394}$. The scatter in the points on OE$_{394}$'s solar phase curve at low phase angles (Figure 5) and at $\alpha = 41°$ (Figure 3) suggests that this large KBO may have a high-amplitude rotation curve, perhaps due to a nonspherical shape and/or surface albedo variations. Since we assume that OE$_{394}$'s color over the LORRI bandpass (350–850 nm) is similar to that of other CCKBOs (Table 2), we apply the Weaver et al. (2020)

color correction for CCKBO Arrokoth, CC = +0.067 mag, to transform LORRI magnitudes to Johnson V.

2.8. Triton

New Horizons LORRI observed Neptune's largest satellite Triton at two epochs in 2019 September at phase angle $\alpha = 79°$ (Table 13). Although Voyager 2's narrow angle camera observed Triton at phase angles between $\alpha = 12°$ and 159° in its green (GRN) filter (centered at 566 nm, near the V filter at 550 nm) during the spacecraft's 1989 August encounter with Neptune (Hillier et al. 1991a), the New Horizons observations help to fill in a gap in the Voyager 2 data set between $\alpha = 67°$ and 133°.

We combine Earth-based, low phase angle observations of Triton in the V filter from $\alpha = 0°.023$ to 1°.15 (Buratti et al. 2011) with high phase angle observations obtained by New Horizons LORRI at $\alpha = 79°$ (Table 13) and Voyager 2's GRN filter from $\alpha = 12°$ to 140° to construct Triton's solar phase curve from $\alpha = 0°.023$ to 140° for comparison with DPs and

Table 13
LORRI Observations of Triton

Observation Mid-time	r (au)	Δ (au)	Sub-s/c Lat. (deg)	Sub-s/c Lon. (deg)	α (deg)	Exposure Time (s)	Total Images	LORRI Magnitude	V Magnitude at 1 au[a]
2019-08-31 08:20	29.933	40.145	+21	282	78.923	1.967	20	15.39 ± 0.1	−0.046
2019-09-02 19:15	29.937	40.167	+21	72	78.926	1.967	20	15.38 ± 0.1	−0.057

Note.
[a] Since Triton's color over the LORRI bandpass (350–850 nm) is similar to that of Pluto (Table 2), we apply the Weaver et al. (2020) Pluto color correction, −0.037 mag, to transform LORRI magnitudes to the Johnson V magnitude of Triton viewed at 1 au from the Sun and 1 au from LORRI.

other large KBOs (Figures 3–5). We do not include the Voyager 2 observations at $\alpha > 140°$ because Triton's atmosphere makes a nonnegligible contribution to the disk-integrated reflectance at these high phase angles and our purpose here is to compare Triton's surface scattering properties with those of the DPs and large KBOs. All Earth-based Triton observations are corrected for variation in reflectance with longitude, using Triton's V-band rotation curve from Buratti et al. (2011) that has a total amplitude 0.052 ± 0.03 mag. The Voyager 2 observations are corrected for rotation using Triton's light curve in the GRN filter that has a total amplitude 0.04 mag (Hillier et al. 1991b). Because New Horizons' two visits were intentionally planned to take place at the maximum and minimum of Triton's rotation curve and longitudes 72° and 282°, respectively, we average the two measurements. The subspacecraft latitudes of the New Horizons LORRI observations, however, are significantly higher than those of the Voyager 2 observations, and no corrections are made to account for any latitudinal variation in reflectance on Triton. Nevertheless, we note that the LORRI observation at $\alpha = 79°$ is consistent with the value predicted by Buratti et al. (2011) in their model disk-integrated phase curve of Triton at the same phase angle. Triton's color over the LORRI bandpass (350–850 nm) is similar to that of Pluto (Table 2); therefore, we apply the Weaver et al. (2020) Pluto color correction, CC = −0.037 mag, to transform LORRI magnitudes to Johnson V.

3. Solar Phase Curve Modeling

Radiation reflected from the surfaces of airless planetary bodies contains information about the physical characteristics of particles that compose the optically active layer of their regolith. Photometric models strive to infer these physical surface properties, including roughness, porosity, particle structure, and size, from the analysis of the phase function, or the manner in which reflected light varies with illumination and viewing geometry. The success with which physical surface properties can be derived from photometric models depends highly on the availability of observations that span the full range of illumination and viewing geometries, from the lowest to the highest solar phase, incidence, and emission angles (Verbiscer & Helfenstein 1998). Typically, filling the entire range of illumination angles requires the availability of both disk-integrated, or full-disk, observations and disk-resolved data. However, the New Horizons LORRI observations of the DPs and large KBOs presented in this work are not spatially resolved. While disk-resolved data are available from close flybys of Pluto, Charon, and Triton, we model only disk-integrated observations of these targets to facilitate comparison with the disk-integrated observations of the other DPs and large KBOs.

Observations at the lowest solar phase angles characterize the opposition effect, or surge, the dramatic, nonlinear increase in reflectance as phase angles approach zero near opposition. Reflectance measurements at moderate to large solar phase angles (e.g., $\alpha > 40°$) and high incidence and emission angles ($>60°$) constrain physical surface characteristics such as the mean topographic slope, or roughness; therefore, disk-resolved data are often required to constrain surface roughness. Observations at extreme phase angles, large ($\alpha > 120°$) and small ($\alpha < 10°$), constrain the directional scattering behavior and particle transparency and opacity.

Combining Earth-based observations acquired at low solar phase angles ($\alpha < 2°$) with those obtained by New Horizons LORRI at higher phase angles ($8° < \alpha < 94°$) enables the production of disk-integrated solar phase curves for the DPs and large KBOs. Figure 3 shows solar phase curves at phase angles $\alpha < 100°$ for each DP, Triton, Charon, Quaoar, MS$_4$, Ixion, and OE$_{394}$, and Figure 4 highlights the near-opposition portions at $\alpha < 2°$ from Earth-based observations. All Earth-based observations except those for Ixion and OE$_{394}$ have been corrected for rotational variation in reflectance (i.e., rotation curve) by removing deviations from the mean reflectance. Because we use data from multiple filters and photometric systems, we apply color corrections (CC) to transform all observations to a single wavelength, here the Johnson V magnitude system (see Sections 2.1–2.8 and Tables 4–13 for details). We normalize all observations to the geometric albedo at opposition. By definition, the geometric albedo is directly related to the size of a body, so the diameter must be either known or estimated. Diameters, and therefore geometric albedos, of all DPs, Quaoar, MS$_4$, and Ixion have been measured by stellar occultations (Table 2). Since the size of OE$_{394}$ is not known, we assume that its geometric albedo $p_V = 0.15$ and colors $B − V$ and $V − R$ are equivalent to those of the average CCKBO (Hainaut et al. 2012; Lacerda et al. 2014; see Table 2). Upon construction of the complete solar phase curves, we fit them to the Hapke (2012b) photometric model using the method of Helfenstein (1986; see Helfenstein & Veverka 1989) but modified following Helfenstein & Shepard (2011). Note that in our adaptation of the Hapke model, at small phase angles (i.e., phase angles smaller than the angular radius of the Sun as seen from the target body) we numerically integrate source intensity over incidence angles that cover the Sun's disk and include a solar limb-darkening approximation. Only Pluto, Triton, and Charon have been observed at phase angles smaller than the angular radius of the Sun (Buratti et al. 2011; Verbiscer et al. 2019a); the smallest phase angles at which the other DPs and large KBOs have been observed are larger than the angular radius of the Sun seen from those targets. We have also adopted an improved error analysis method (Helfenstein & Verbiscer 2022, in preparation)

that, in addition to the standard goodness-of-fit errors, includes a percent measure that characterizes the sensitivity to which available coverage constrains each retrieved parameter. Moreover, we especially use this measure, called the effective geometry constraint (C_{EG}), to indicate how the absence of phase angle coverage beyond the observed range imposes limits on the reliability of each parameter retrieval (see Section 3.1.1).

3.1. Hapke Photometric Parameters

The Hapke (2012b) bidirectional reflectance equation models the radiance factor, $r(i, e, \alpha)$, scattered from a particulate surface element, illuminated from incidence angle i, and viewed at emission angle e and solar phase angle α:

$$r(\alpha, \mu_o, \mu) = K \frac{\tilde{\omega}_o}{4} \frac{\mu'_o}{(\mu' + \mu'_o)}$$
$$\times \left[(1 + B_{oS}(\alpha))P(\alpha) + M_s\left(\tilde{\omega}_o, \frac{\mu'}{K}, \frac{\mu'_o}{K}\right) \right]$$
$$\times [1 + B_{oC}(\alpha)] S(\mu'_o, \mu', \alpha, \bar{\theta}),$$
(3)

where $\tilde{\omega}_o$ is the average particle single-scattering albedo, K is a porosity coefficient, $B_{oS}(\alpha)$ is the Hapke (2012b) function that describes the shadow-hiding opposition effect (SHOE), $P(\alpha)$ is the average single particle phase function (SPPF), and $M_s\left(\tilde{\omega}_o, \frac{\mu'}{K}, \frac{\mu'_o}{K}\right)$ models the contribution from interparticle incoherent multiple scattering. $B_{oC}(\alpha)$ is a function that describes the coherent backscatter opposition effect (CBOE). In this work we apply the Helfenstein & Shepard (2011) version of the Hapke (2012b) model that relates K to the angular width of the SHOE through the regolith porosity, eliminating the need to solve for K explicitly. The quantities μ_o and μ are the cosines of the incidence angle (i) and emission angle (e), respectively, and primes on these symbols indicate that they are the *effective* cosines of i and e, corrected for the effects of macroscopic roughness. Finally, $S(\mu'_o, \mu', \alpha, \bar{\theta})$ models the shadowing due to photometric roughness, where $\bar{\theta}$ represents the mean topographic slope angle of surface relief at resolutions below the pixel scale of the observations. We describe each parameter in detail below; for more detailed descriptions, see reviews by Verbiscer & Helfenstein (1998) and Verbiscer et al. (2013).

The single-scattering albedo $\tilde{\omega}_o$ is defined as the ratio of particle scattering to extinction efficiencies and is related to particle composition, size, and microstructure. The opposition effect, or surge, is the product of two phenomena: interparticle shadow hiding and a constructive interference phenomenon known as coherent backscatter (Shkuratov 1988; Muinonen 1990). Two parameters describe both the SHOE and the CBOE: an angular width h expressed in radians and an amplitude B_o. The SHOE angular width h_S is related to surface particle porosity and size distribution. The SHOE amplitude B_{oS} is related to particle transparency; it is the fraction of light backscattered directly from the front surface of a particle relative to the total amount of light scattered in the backward direction. For perfectly opaque particles, $B_{oS} = 1$. The CBOE angular width h_C and amplitude B_{oC} depend on the density and

size of small scatterers and the mean optical path length of a photon (medium transparency). The amplitudes of both the SHOE B_{oS} and CBOE B_{oC} have upper limits of unity.

For most DPs and large KBOs, we apply a two-parameter Henyey & Greenstein (1941) SPPF, which is a linear combination of two single-parameter Henyey–Greenstein functions (McGuire & Hapke 1995):

$$P(\alpha; b, c) = \frac{(1 + c)}{2} \frac{(1 - b^2)}{(1 - 2b\cos(\alpha) + b^2)^{3/2}}$$
$$+ \frac{(1 - c)}{2} \frac{(1 - b^2)}{(1 + 2b\cos(\alpha) + b^2)^{3/2}}.$$
(4)

The b parameter is the (assumed to be equal) angular width of the backward- and forward-scattering lobes of the particle phase function, and the c parameter is the relative amplitude of each lobe. Values of the b parameter are limited to $0 \leqslant b < 1$, and values of c are limited to

$$|c| \leqslant \frac{1 + 3b^2}{b(3 + b^2)}$$
(5)

because $P(\alpha; b, c)$ cannot be negative and has extremes at $\alpha = 0°$ and $180°$ (Hapke 2012b). These two parameters characterize the mechanical structure of surface grains: surfaces with $b > 0.5$ have euhedral, smoother particles, and surfaces with $b < 0.5$ have irregularly shaped, rougher particles. Similarly, particles with $c > 0$ have higher densities of internal scatterers and are more opaque, while particles with $c < 0$ have a lower density of internal scatterers and are thus more transparent. Observations at extreme phase angles, both large and small, constrain the SPPF b and c parameters; however, since the phase angle range is limited for Eris, we apply a single-parameter SPPF with the c parameter fixed at $c = -1.00$ to that data set. For 2002 MS$_4$, the value of the c parameter is calculated using the Hapke (2012a) empirical hockey stick relation (Table 14, footnote c).

The incoherent multiple reflection of light within the regolith medium is controlled by both the average particle single-scattering albedo and the directional scattering of light characterized by the SPPF. In this study, we have adopted the Hapke (2012b) model for anisotropically scattering grains.

3.1.1. Model Fitting and Error Analysis

For nearly all DPs and large KBOs, the solar phase angle coverage of observations is highly nonuniform, most often with a disproportionately large number of Earth-based observations at small phase angles and only a few widely spaced data points from New Horizons LORRI at larger phase angles, seldom with $\alpha > 90°$. Consequently, our approach takes into consideration the likely nonuniqueness of model solutions. In these cases, we have adopted a special strategy for fitting the phase curve data and then performed error analyses on the results. Our motivation for choosing the Hapke (2012b) model is threefold. The first and highest priority is to model the phase curve behavior as accurately as possible for the purpose of estimating phase integrals and Bond albedos. Extrapolation of the phase curves beyond the range of coverage, as well as interpolation between large gaps, is critical and best facilitated by physically based models rather than empirical approximations. A secondary priority is to interpret the best-constrained model

Table 14
Hapke ([2012b](#)) Parameters for Dwarf Planets, Satellites, and Large KBOs Observed by New Horizons

Object	Single-scattering Albedo $\tilde{\omega}_o$	Photometric Roughness[a] $\bar{\theta}_p$ (deg)	SPPF b	SPPF c	SHOE Width h_S	SHOE Amplitude B_{oS}	CBOE Width h_C	CBOE Amplitude B_{oC}
Eris	$0.99\overline{9}$	(20)[b]	0.95	(-1.00)[b]	⋯	⋯	0.057	0.36
Makemake	0.947	5	0.73	-0.88	0.11	1.00	⋯	⋯
Haumea	0.625	(20)	0.39	0.00	0.22	0.99	0.074	0.32
Quaoar	0.145	(20)	0.36	-0.54	0.50	0.18	0.051	1.00
2002 MS$_4$	0.103	(20)	0.31	$[-0.30]$[c]	0.24	1.00	0.076	1.00
Ixion	0.065	(20)	0.24	1.55	0.14	0.98	0.089	0.72
2014 OE$_{394}$	0.211	34	0.08	1.98	0.025	0.90	0.032	1.00
Triton[d]	$0.99\overline{9}$	27	0.63	-0.94	0.495	0.47	0.00055	0.17
Pluto[e]	0.917	28	0.60	-0.77	0.035	0.21	0.00014	0.18
Charon[f]	0.485	23	0.059	1.950	0.19	1.00	0.0047	0.47

Notes.
[a] The mean photometric roughness $\bar{\theta}_p$ differs from the macroscopic roughness $\bar{\theta}$. See Section [4.6](#) for details.
[b] Values in parentheses were held fixed during the Hapke model fit.
[c] Value of the c parameter in brackets was computed from the b parameter that was fit using Hapke's empirical hockey stick relation: $c = 3.29 \exp(-17.4b^2) - 0.908$ (Hapke [2012a](#)).
[d] We refit New Horizons LORRI data (Table [13](#)) and the Voyager 2 data from Hillier et al. ([1990](#), [1991a](#)) and the V-filter near-opposition data from Buratti et al. ([2011](#)), corrected to the reflectance of Triton at longitude 0° and 180°, i.e., Triton's rotation curve. To correct for residual instrumental calibration differences between the three data sets, we empirically determine offsets of $+0.061$ mag for Voyager 2 and $+0.116$ mag for LORRI to normalize them relative to the V-filter near-opposition data. We fit to a two-parameter, rather than a single-parameter, SPPF for ease of comparison with DPs and large KBOs.
[e] We refit the HST Pluto data from Verbiscer et al. ([2019a](#)) that have been adjusted to $\lambda_{\rm eff} = 555$ nm and corrected them to Pluto's reflectance at longitude 0° and 180°. We also include composite phase curve New Horizons LORRI and Multispectral Visible Imaging Camera (MVIC; Reuter et al. [2008](#)) data from Hillier et al. ([2021](#)), offset by $+0.47$ mag to normalize them relative to the HST near-opposition data, excluding observations at phase angles $\alpha > 115°$ that contain strong contributions from Pluto's haze layer. These parameters differ from and supersede those reported by Verbiscer et al. ([2019a](#)) and Olkin et al. ([2021](#)), where only a single SPPF was used and the CBOE multiplied contributions from multiple scattering only, not contributions from both multiple and single scattering. The Hapke parameter set for Triton was used as a good first approximation to model Pluto from which all of the Hapke parameters were subsequently allowed to adjust to relatively small differences in the phase curves. See text and [Appendix](#) for discussion.
[f] We refit the Charon data from Howett et al. ([2021](#)) with a two-term SPPF rather than a single term for ease of comparison with DPs and large KBOs.

parameters to gain insight about surface physical properties of the regoliths covering the bodies. Finally, modeling of spectroscopic measurements relies on accurate knowledge of the Hapke parameters that characterize a planetary surface. In particular, Verbiscer et al. ([2006](#)) demonstrated that use of an incorrect SPPF can lead to erroneous conclusions about the abundance of end member components, and therefore the composition, of a planetary surface.

Preliminary model fitting trials using standard χ^2 minimization resulted in pathological fits because of an asymmetric distribution of data point density with phase angle, strong contrasts in estimated observation uncertainties that correlated with phase angle, or a high degree of data scatter at selective portions of the phase curve. To minimize the skew and best ensure that the optimal fit matched data points over the full phase angle range of observations, we performed the parameter fits directly on a magnitude scale and without any statistical weighting. However, once the fits were obtained, we use the reported observation uncertainties to compute goodness-of-fit parameter uncertainties.

The computation of goodness-of-fit errors is especially problematic for our data sets. To begin, the standard χ^2 approaches for determining the confidence envelope around each model parameter require that the model parameters be independent variables. This is not the case for the Hapke ([2012b](#)) model, in which the parameters are not independent, but are often coupled to each other by a mutual dependence on more fundamental physical attributes of the scattering medium (see Protopapa et al. [2020](#)). In addition, we are working with

data sets for which we often have almost as many model parameters as data points, so that the occurrence of multiple, nonunique parameter solutions requires special attention. A further complication is that observation uncertainties from different data sources may not have been determined in a mutually consistent way; they may exclude sources of error such as uncertainties due to imperfect rotation curve corrections, uncertainties in the projected area of distant targets, and instrumental uncertainties that may vary with observation geometry and observing conditions. Consequently, reported observation uncertainties may significantly under- or overestimate values relative to the observations on a scale that is appropriate to determine a meaningful error envelope around each solved parameter with a standard approach, such as the $\Delta\chi^2 = 1$ for one free parameter and a 68% confidence level.

Violating the requirement that the model parameters be independent variables severely limits the applicability of routine error estimation methods to our analysis (Andrae [2010](#); Andrae et al. [2010](#)). Our Hapke ([2012b](#)) model fitting software (see Helfenstein & Verbiscer 2022, in preparation) lends itself to addressing these issues. Among its capabilities, it allows an incremental stepwise grid search to be performed over valid ranges of any given parameter, while the remaining parameters are allowed to adjust via a gradient-following algorithm to any incremental change in the grid-searched parameter. Note that this approach differs from that in the case of independent variables, for which a stepwise grid search is performed, while the remaining parameters are fixed throughout the search. By doing so, our stepwise grid-search algorithm addresses the

coupling between model parameters. Upon finding a nominal fit of the Hapke (2012b) model to phase curve observations, we perform the stepwise grid search over the full range around each model parameter to accumulate a database of *relative* χ^2 residuals. The grid-search database likely contains multiple solutions. Many of the nonunique solutions can be excluded on the basis that coupling of the Hapke (2012b) parameters often leads to a condition where one component of the function, such as the SPPF, can mimic the behavior of another, such as the shadow-hiding opposition surge. After applying the exclusion criteria to the database, the remainder of the grid-search residuals are analyzed by histogram relative to the best-fit solution. The histogram analysis provides a 1σ "base water-line" in χ^2 space below which all of the goodness-of-fit parameter solutions are statistically the same. Goodness-of-fit error bars for each parameter are determined from the statistical collection of all fits below the waterline level.

However, goodness-of-fit uncertainties are poor measures of confidence, since they do not account for the extent to which a given model parameter may actually be constrained by the available observations (or be unconstrained by missing coverage). To account for the absence of observations over broad ranges of phase angle, we compute a second measure of confidence termed "effective geometry constraints" (Helfenstein & Verbiscer 2022, in preparation) based on earlier work (Helfenstein et al. 1988) that tests the extent to which available observations constrain each parameter in the fitted model. The effective geometry constraint is given on a percent scale for which 100% indicates that the model parameter was fully constrained. Note that some model parameters, such as narrow coherent backscatter opposition effect widths, can be fully constrained with only a few degrees worth of phase angle coverage (see Table 15). We have used the effective geometry constraint as an additional factor for interpreting the reliability of our model parameter error estimates.

The overall fitting process is often iterative, especially when the effective geometry constraint for a given parameter, such as macroscopic roughness $\bar{\theta}$, indicates that it is not constrained at all by the available phase angle coverage. In those cases, we will often fix the unconstrained parameter at a plausible value (e.g., $\bar{\theta} = 20°$). This approach also reduces the number of model parameters in cases where we have as many or more model parameters than data points. To further reduce the number of model parameters, for MS_4 we adopted a one-parameter variant of the SPPF such as Hapke's "hockey stick" (Hapke 2012a) empirical approximation or a single-parameter Henyey–Greenstein function owing to limited phase angle coverage.

We found that for the bright objects, Eris, Triton, and Pluto, it was necessary to adopt a single-parameter Henyey–Greenstein function because the particle phase function has a solitary narrow forward-scattering lobe that was being mirrored as a pseudo-opposition surge at small phase angles by the symmetry assumptions inherent in the McGuire–Hapke SPPF. In these cases, to convert the McGuire–Hapke function effectively to a single-parameter forward-scattering Henyey–Greenstein function, we fixed the c parameter at -1.0. Because of their more complete phase angle coverage, in subsequent fits to Triton and Pluto we were able to use our first fits as first approximations and then to relax the requirement, finding that the retrieved values of the c parameter did not deviate much from -1.0.

4. Results

Table 14 summarizes the sets of Hapke parameters derived from fits to the solar phase curves for each DP and large KBO in this study, and Table 15 lists the corresponding uncertainties and effective geometry constraints for each model parameter. The effective geometry constraint represents the percent of solar phase angle coverage needed to constrain the least-squares fit of a given Hapke (2012b) model parameter. The solid lines in Figures 3–5 are the Hapke (2012b) model fits to the disk-integrated solar phase curves for each DP and large KBO in this study. Each phase curve in Figures 3–5 is normalized to magnitude zero at opposition to facilitate comparison between shapes of the phase functions of all DPs, large KBOs, Charon, and Triton. Figure 6 presents the Hapke parameters in Table 14 with their corresponding uncertainties from Table 15 in graphical form.

4.1. Single-scattering Albedos

Since the sizes and shapes of the DPs, satellites, and many large KBOs are well known from stellar occultations, space-craft flybys, or both, one expects their single-scattering albedos to be likewise well constrained. This is not the case, however, since the single-scattering albedo is intimately coupled to the *full* shape of the average SPPF; therefore, to constrain the single-scattering albedo well, one must fully constrain the SPPF. Fully constraining the SPPF requires observations over the full range of solar phase angles because a relatively narrow forward-scattering lobe of the SPPF may be present. In that case, if there are no observations at high α, the undetected forward-scattering spike, like that which occurs in transparent frosts and icy grains, would yield an underestimated value of the single-scattering albedo. Thus, for surfaces containing significant exposures of bright icy particles, the paucity of reliable, high-quality, high-α observations could introduce high uncertainties in $\tilde{\omega}_o$. Low to moderate albedo surfaces may lack strong forward-scattering lobes in the SPPF, so for dark regoliths the absence of high-α observations may not introduce large uncertainties in the single-scattering albedo.

Single-scattering albedos in Table 14 range widely, from $\tilde{\omega}_o = 0.065 \pm 0.005$ for Ixion to $\tilde{\omega}_o = 0.99\overline{9}$ for Eris and Triton. Our derived single-scattering albedo for OE_{394}, $\tilde{\omega}_o = 0.211 \pm 0.064$, is modestly constrained; however, recall that its phase curve has been normalized to an assumed geometric albedo, the average geometric albedo for all CCKBOs (Lacerda et al. 2014). Until a diameter is determined for OE_{394}, either by stellar occultation or by thermal radiometric measurements, its geometric albedo, single-scattering albedo, and Bond albedo can only be estimated using the average p_V for CCKBOs.

4.2. Opposition Effect Parameters

The opposition effect parameters, namely, the angular width and amplitude of the SHOE and the CBOE, are largely constrained by Earth-based observations at low phase angles. Table 3 reports the range of solar phase angles at which these DPs, satellites, and large KBOs have been observed from Earth. The CBOE acts on the smallest solar phase angles, $\alpha < 2°$, and New Horizons has not observed any DPs or KBOs at phase angles $\alpha < 8°$. The SHOE's photometric behavior is observed over phase angles that can extend to tens of degrees (Helfenstein et al. 1997). New Horizons observed Makemake

Table 15

Uncertainties and Effective Geometry Constraints[a] in Hapke (2012b) Parameters for Dwarf Planets, Satellites, and Large KBOs Observed by New Horizons

Object	$\tilde{\omega}_o$	$\bar{\theta}_p(°)$ [b]	SPPF b	SPPF c	SHOE Width h_S [c]	SHOE Amplitude B_{oS}	CBOE Width h_C [d]	CBOE Amplitude B_{oC}	χ^2 Residual	χ_w^2 Residual[e]
Eris	$^{+0.000}_{-0.003}$	$^{+23}_{-20}$	$^{+0.05}_{-0.84}$	...	...	...	±0.009	±0.04	0.296	0.316
	[14]	[<1]	[<1]	[27]	[<1]	[<1]	[5]	[23]		
Makemake	$^{+0.053}_{-0.127}$	$^{+10}_{-5}$	$^{+0.27}_{-0.51}$	$^{+1.89}_{-0.13}$	$^{+0.13}_{-0.11}$	$^{+0.00}_{-0.17}$	...	...	2.22	3.58
	[20]	[< 1]	[16]	[88]	[20]	[87]	[–]	[–]		
Haumea	±0.116	$^{+30}_{-20}$	±0.06	±0.42	±0.13	$^{+0.01}_{-0.12}$	$^{+0.125}_{-0.074}$	±0.30	0.346	0.401
	[24]	[34]	[37]	[39]	[34]	[78]	[80]	[99]		
Quaoar	±0.028	$^{+23}_{-20}$	±0.05	±0.06	$^{+0.02}_{-0.07}$	±0.06	±0.008	$^{+0.00}_{-0.39}$	0.834	1.682
	[25]	[2]	[21]	[9]	[24]	[23]	[41]	[8]		
2002 MS$_4$	±0.023	±2	±0.01	$^{+0.43}_{-0.28}$ [g]	±0.07	$^{+0.00}_{-0.21}$	±0.011	$^{+0.00}_{-0.13}$	0.046	0.085
	[23]	[< 1]	[8]	[19]	[26]	[26]	[3]	[21]		
Ixion	±0.005	$^{+30}_{-20}$	±0.06	±0.03	±0.13	$^{+0.02}_{-0.06}$	±0.007	±0.07	0.175	0.191
	[8]	[<1]	[<1]	[<1]	[10]	[11]	[2]	[29]		
2014 OE$_{394}$	±0.064	±14	$^{+0.16}_{-0.08}$	$^{+0.02}_{-1.21}$	$^{+0.039}_{-0.014}$	±0.04	$^{+0.012}_{-0.032}$	$^{+0.00}_{-0.08}$	3.491	3.886
	[10]	[1]	[3]	[3]	[10]	[17]	[39]	[7]		
Triton	$^{+0.000}_{-0.089}$	±9	± 0.32	$^{+0.82}_{-0.41}$	$^{+0.027}_{-0.033}$	±0.28	$^{+0.00566}_{-0.00024}$	±0.04	0.846	9.248
	[26]	[8]	[1]	[33]	[7]	[24]	[99]	[92]		
Pluto	$^{+0.083}_{-0.140}$	±5	±0.12	±0.23	$^{+0.172}_{-0.035}$	$^{+0.42}_{-0.21}$	$^{+0.00023}_{-0.00000}$	±0.13	17.8	45.1
	[51]	[3]	[3]	[30]	[17]	[16]	[<1]	[<1]		
Charon	±0.038	<1	$^{+0.110}_{-0.060}$	$^{+0.002}_{-0.926}$	±0.09	$^{+0.00}_{-0.14}$	±0.0004	±0.01	1.758	4.788
	[11]	[5]	[9]	[8]	[13]	[20]	[97]	[97]		

Notes.

[a] Values within brackets are the effective geometry constraints C_{EG} for each model parameter, expressed as percentages. These represent the percent of phase angle coverage needed to fully constrain the least-squares fit of a given model parameter, where 100% indicates that the parameter is fully constrained, and small percentages indicate that a parameter is poorly constrained.

[b] Uncertainties in cases for which $\bar{\theta}_p$ was fixed at 20° were determined from a stepwise grid search of values covering a range of 0°−60°, with 50° being considered here as an upper physical limit (Helfenstein & Verbiscer 2022, in preparation).

[c] For h_S, the absolute upper limit is $h_S = 0.522$ (Hapke 2012b). For the absolute lower limit on h_S we require that the angular width of the SHOE be greater than or equal to one-third of the CBOE angular width, $h_S \geqslant 0.33h_C$ (Helfenstein & Verbiscer 2022, in preparation). For Makemake, the value of h_C is indeterminate, so we assumed a lower limit equal to the value h_S would be if its HWHM were equal to the angular width of the solar disk.

[d] For Haumea, 2014 OE$_{394}$, Pluto, and Triton, the statistically computed lower limits on h_C were unphysical. In the first three cases, the lower limits were set by requiring that the angular HWHM values be at least as large as the angular radius of the solar disk. Because the detection of the CBOE also depends on its amplitude and the surface albedo, this criterion is imperfect. Triton's retrieved h_C value was narrower than the solar disk criterion. In that case, we set the lower limit to the precision level of its retrieved h_C.

[e] χ_w^2 defines the base margin χ^2 ("waterline") above and below which Hapke parameter solutions do not statistically differ. It determines the contribution of the goodness-of-fit errors to the parameter value uncertainties.

[f] Ellipses denote not applicable uncertainties or effective geometry constraints.

[g] As noted in Table 14, the value of the SPPF c parameter was computed directly from the SPPF b parameter, and the error estimate is derived from the corresponding error limits for the SPPF b.

and Haumea at $\alpha = 8°$, and these LORRI observations provide significant constraints on the SHOE amplitude and width compared to our other DPs and KBOs (see Tables 15 and 16). Since corrections for the rotational variation in reflectance (light curve) have been applied to the low phase angle observations of Eris, Makemake, Haumea, and Quaoar, the opposition effect parameters for these objects are as constrained as they possibly can be, given the limitations in the minimum phase angle at which they can be observed. Makemake and Haumea, for instance, have never been observed at $\alpha < 0°.5$, so the opposition effect parameters for these DPs are not as well constrained as those for Ixion, Eris, and Quaoar, which have been observed at smaller phase angles. Although 2002 MS$_4$ has a low-amplitude light curve (Thirouin 2013), the sparse sampling of its Earth-based observations only approximates the amplitude and width of its opposition effect. Without corrections to the rotation curve at low phase angles, the opposition effect amplitudes and angular widths are not at all

well constrained for objects that may have high-amplitude light curves such as OE$_{394}$.

Table 16 lists the regolith porosity ranges implied by our best-fit Hapke SHOE angular widths from Tables 14 and 15 using the relationship $h_s = -0.3102\phi^{1/3}\ln(1 - 1.209\phi^{2/3})$ (Hapke 2008) to calculate the porosity p where the filling factor $\phi = (1 - p)$. In some cases, the statistically computed lower limit to h_s was negative or zero. SHOE solutions with a lower uncertainty limit of $h_S = 0$ correspond to a physically unrealistic porosity of 100%. In these cases, we assumed that the angular half-width at half-maximum (HWHM) of the SHOE had to be at least as large as that of the CBOE, because the physical mechanisms that control the SHOE operate on size scales that overlap but are typically much larger than those from which the CBOE arises. This assumption also limits the ambiguity that can arise when the angular width of the SHOE is so narrow that $h_S \approx h_C$, in which the SHOE mimics the CBOE. SHOE solutions with an upper uncertainty limit of $h_S = 0.522$
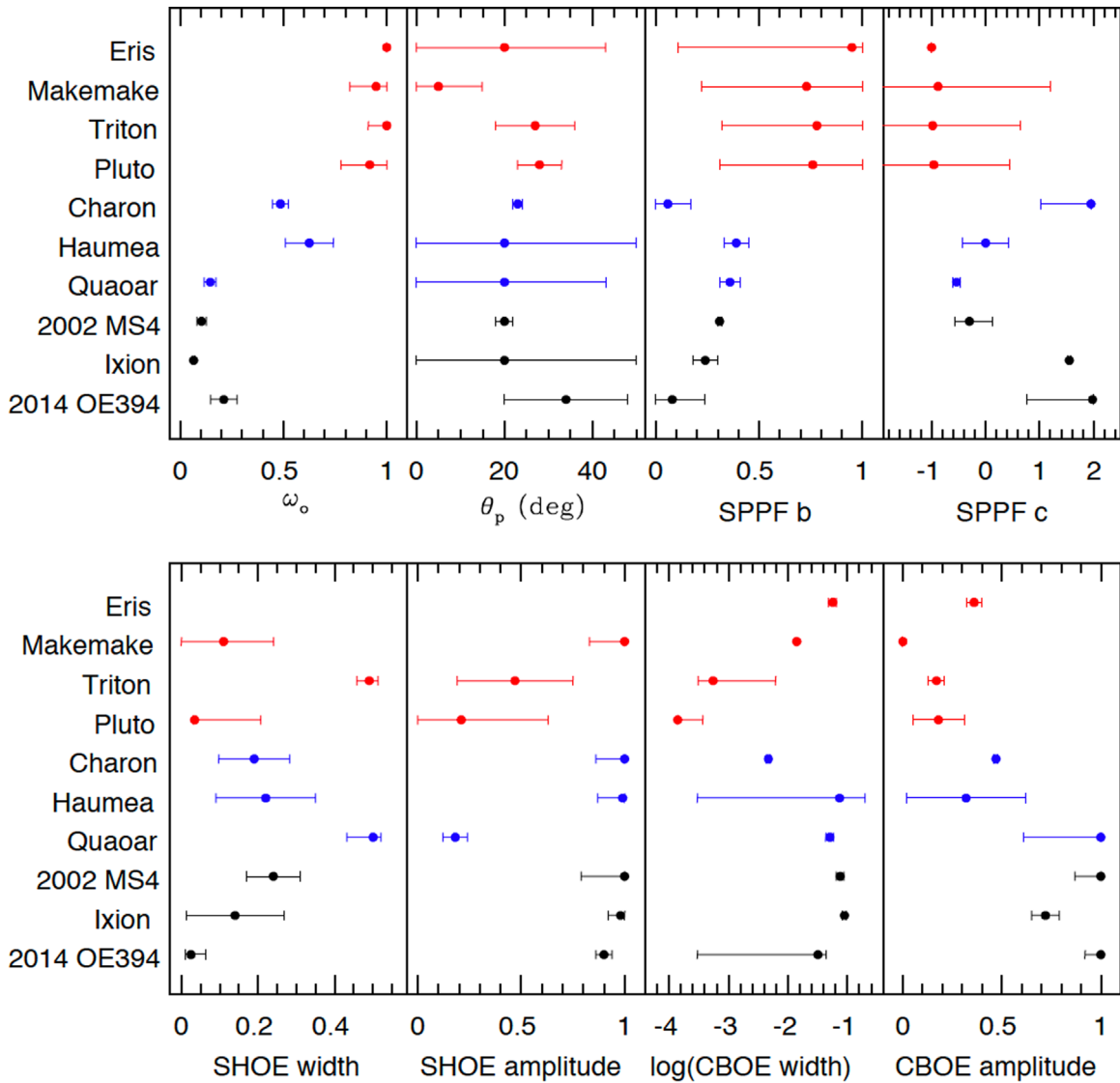
Figure 6. Hapke parameters from Table 14 with uncertainties from Table 15. For the objects in red, hypervolatiles such as N$_2$ and CH$_4$ play major roles in their surface composition. For the objects in blue, water ice plays a major role in their surface composition. Black circles correspond to parameters for objects with surface compositions dominated by nonvolatiles.

are required by the assumption of the Hapke (2012b) compaction model that regolith particles be separated far enough that grain packing does not produce significant coherent-interference compaction effects. It is physically possible for regolith grains to be packed below this limit so that the true lower porosity limit is ambiguous.

Table 15 shows that the SHOE parameters are often significantly less well constrained than those for the CBOE. This condition is largely a consequence of the fact that the angular half-width of the SHOE can extend tens of degrees beyond the phase angle coverage of Earth-based observations to a range where New Horizons data points are relatively sparse. Moreover, the angular half-width of the SHOE extends to a range for which the macroscopic roughness and particle phase function behavior can mimic the SHOE and introduce ambiguities (Helfenstein & Verbiscer 2022, in preparation).

The regolith porosity ranges for Haumea and Quaoar are in broad agreement with those of Triton and Charon, each of which has a higher degree of effective phase angle coverage.

The angular width of the CBOE provides an approximate measure of regolith maturity in which increasing angular

widths (i.e., larger values of h_C) represent regoliths with increasing maturity (Hapke 2021). The bar chart in Figure 7 shows the value of h_C for each object in increasing order of the angular width. The diagram implies that Triton and Pluto, two of the objects with the highest albedos, have the least evolved regoliths, while the lowest-albedo objects (Ixion, 2002 MS$_4$, Quaoar, and 2014 OE$_{394}$) are among the objects with the most evolved regoliths. Charon, which has an intermediate albedo, has a surface that is also intermediate in maturity.

4.3. Single Particle Phase Functions

The SPPF parameters b and c vary greatly among these DPs and large KBOs. Plots of b versus c for particles of different transparencies and shapes occupy a parameter space that is restricted to values yielding a shape resembling a hockey stick (Hapke 2012a). Figure 8 shows such a "hockey stick" plot for the DPs, satellites, and other DKBOs observed by New Horizons. The empirical hockey stick relation (the thick solid curve in Figure 8) approximates the behavior of a broad range of particulate surfaces and may be considered a first-order model
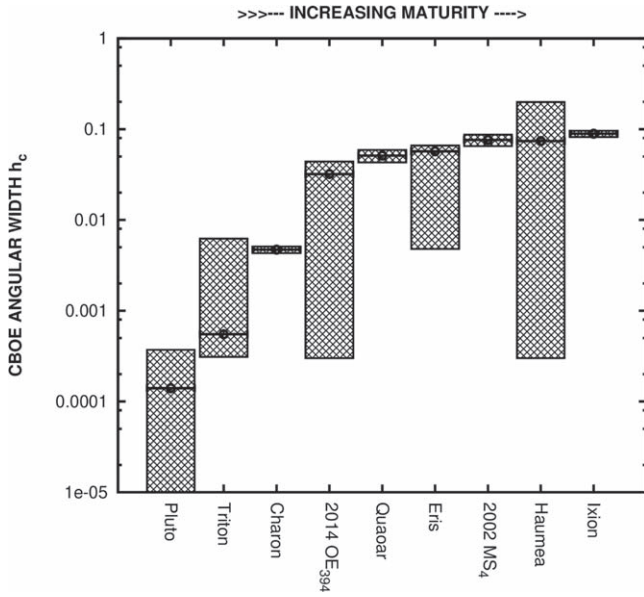
Figure 7. Floating bar chart showing the nominal values of the CBOE h_C parameters (circles with center bars) from Table 14 arranged in order of increasing angular width. The corresponding uncertainty ranges (from Table 15) are indicated by shaded boxes. Relative regolith maturity for each object is interpreted to increase from left to right in the plot. Note that the vertical scale is logarithmic. Makemake has been excluded because its available phase angle coverage was insufficient to constrain h_C in our Hapke model fit. The two leftmost bodies (Triton and Pluto) have hypervolatile-rich surfaces. Of the six rightmost bodies, four are low-albedo objects with nonvolatile surfaces (Ixion, 2014 OE$_{394}$, 2002 MS$_4$) or H$_2$O-rich surfaces (Quaoar). Charon's surface is also H$_2$O-rich but is intermediate in maturity. The remaining bodies, H$_2$O-rich Haumea and hypervolatile-rich Eris, appear to have anomalously high albedo surfaces in comparison to the other bodies of similar maturity, although with large uncertainties.

Table 16
Implied Regolith Porosities of Dwarf Planets, Satellites, and Large KBOs Observed by New Horizons

Object	SHOE h_S (rad)	SHOE HWHM (deg)	C_{EG}[a] (%)	Hapke K Parameter	Regolith Porosity[b] (%)
Makemake[c]	$0.11^{+0.13}_{-0.11}$	13	20	$1.00 - 1.66$	78^{+22}_{-20}
Haumea	0.22 ± 0.13	25	34	$1.27 - 1.88$	63^{+18}_{-13}
Quaoar	$0.50^{+0.02}_{-0.07}$	57	24	$2.07 - 2.30$	41^{+4}_{-1}
2002 MS$_4$	0.24 ± 0.07	30	26	$1.46 - 1.78$	60^{+9}_{-7}
Ixion	0.14 ± 0.13	16	10	$1.06 - 1.69$	73^{+24}_{-16}
2014 OE$_{394}$	$0.025^{+0.039}_{-0.014}$	3	10	$1.06 - 1.21$	94^{+3}_{-8}
Triton[c]	$0.495^{+0.027}_{-0.033}$	56	7	$2.15 - 2.31$	41 ± 2
Pluto[c]	$0.035^{+0.172}_{-0.035}$	4	17	$1.00 - 1.54$	92^{+8}_{-28}
Charon	0.19 ± 0.09	22	13	$1.30 - 1.71$	66^{+13}_{-10}

Notes.
[a] Effective geometry constraint (see text).
[b] Values of the porosity, p, are calculated from the SHOE angular width using $h_s = -0.3102\phi^{1/3} \ln(1 - 1.209\phi^{2/3})$, where the filling factor $\phi = (1-p)$ (Hapke 2008).
[c] For the purpose of computing lower limits on the regolith porosity for Makemake, Triton, and Pluto, we assumed that the HWHM can be no smaller than the angular diameter of the Sun viewed from each object.

of most of the particles found in planetary regoliths. With the exception of Ixion and Haumea, all of the bodies in this study fall close to the empirical hockey stick curve. The highest-albedo objects, Triton, Eris, Makemake, and Pluto, all occupy a region of
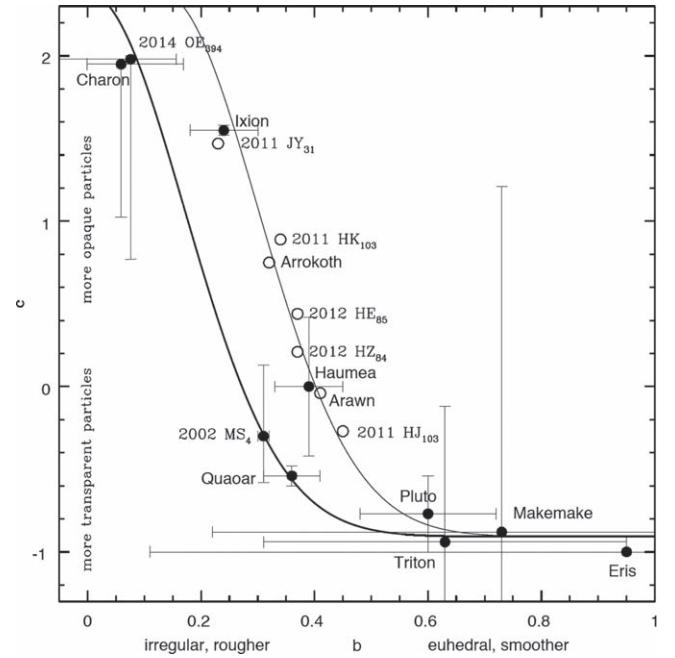
Figure 8. A McGuire & Hapke (1995) "hockey stick" plot showing SPPF c vs. b parameters for all DPs, satellites, and DKBOs observed by New Horizons. Filled circles are objects studied in this work; open circles are the smaller, darker DKBOs studied by Verbiscer et al. (2019b), which include cold and hot classical KBOs, Plutinos, and scattered disk and resonant objects. The thick solid curve is Hapke's empirical "hockey stick" relation (Hapke 2012a), $c = 3.29 \exp(-17.4b^2) - 0.908$, that approximates the behavior of a broad range of particulate surfaces and may represent most particles found in planetary regoliths. The surfaces of the smaller DKBOs are more back-scattering than those of the DPs. This more strongly backscattering behavior parallels the hockey stick curve as shown as a solid thin curve, but the trend is shifted toward characteristics of smoother, more euhedral particles, b values, by 0.13 ± 0.01. This trend is characteristic of many low-albedo solar system bodies.

the plot that characterizes highly transparent, smooth-surfaced grains similar to grains of terrestrial frost and certain classes of snow. Charon and OE$_{394}$ both similarly fall in a region of the plot that characterizes rough, irregularly shaped grains with unusually high densities of internal scatterers. 2002 MS$_4$ and Quaoar similarly fall along the curve over a range of b between 0.30 and 0.35 that is typical of many regoliths on airless planetary bodies in the solar system. However, their regolith grains are generally more transparent than those on most airless, silicate-regolith-coated bodies.

While Ixion and Haumea are significantly offset from the hockey stick curve, they both closely follow a separate trend that characterizes large KBOs and the other smaller New Horizons DKBOs studied by Verbiscer et al. (2019b). That trend is defined by a thin line in Figure 8, which parallels the thick hockey stick curve, but the trend is shifted toward characteristics of smoother, more euhedral particles, b values, by 0.13 ± 0.01. Other dark, airless solar system bodies also follow this trend (Verbiscer et al. 2019b), and Ixion, with its low albedo, has values of b that also fall in the typical range for dark, silicate-regolith-covered bodies. Haumea's higher-albedo grains are also significantly more transparent than for the darker objects.

The SPPF angular widths b span a wide range, from $0.08^{+0.16}_{-0.08}$ for OE$_{394}$ to $0.95^{+0.05}_{-0.84}$ for Eris, indicating that particle structures on DP and large KBO surfaces differ significantly. The SPPF amplitudes c also span a broad range, from $-0.94^{+0.82}_{-0.41}$ for Triton

to $1.98^{+0.02}_{-1.21}$ for OE_{394}, indicating that particles on these objects vary in their relative opacities.

Some caution should be exercised when interpreting SPPFs derived from disk-integrated phase curves of nonspherical objects. Based on several stellar occultation results (e.g., Ortiz et al. 2017), Haumea certainly has a nonspherical shape, and although we have corrected Haumea's disk-integrated reflectances for variation with rotation phase, we have not accounted for the effects of nonsphericity in the analysis of its solar phase curve. Recent stellar occultations by 2002 MS$_4$ indicate that it also has a nonspherical shape (Levine et al. 2021). Given the large variation in the reflectance of 2014 OE$_{394}$ at high phase angles, it is highly likely that this large KBO is also nonspherical. Li et al. (2003, 2004) have shown that assuming a spherical shape for asteroids such as (433) Eros may introduce significant errors, especially at high phase angles, resulting in more forward-scattering phase functions than actually exhibited. Hillier et al. (2011) also found this effect to be true in their analysis of main belt asteroid (5535) Annefrank by the Stardust spacecraft.

4.4. Macroscopic Roughness

We initially held the mean photometric roughness to a fixed value, $\bar{\theta}_p = 20°$, for all the objects when performing fits. Satisfactory fits for all but five objects (those with $\bar{\theta}_p$ values in parentheses in Table 14) were obtained without invoking the roughness parameter. However, for Makemake, OE$_{394}$, Triton, Pluto, and Charon, we relaxed this restriction and obtained significantly improved fits. The mean photometric roughness slope angles for all objects in this study range from $\bar{\theta} = 5°$ for Makemake to $34° \pm 14°$ for OE$_{394}$. We note that the solar phase angle coverage for Eris and Makemake lacks any observations at phase angles larger than $\alpha = 28°$ and $32°$ for each DP, respectively. Photometric roughness estimates for Haumea, Quaoar, MS$_4$, and OE$_{394}$ are better constrained by the LORRI observations of these objects at phase angles between $\alpha = 38°$ and $94°$ (Tables 6, 7, 9, and 12).

4.5. Regolith Grain Transparency and Particle Scattering Asymmetry

Properties that affect the photometrically detectable transparency of regolith grains include composition, grain-size distribution, grain shape and aggregation, the density of scatterers within the regolith grains, and heterogeneity of the surface at both microscopic and macroscopic scales. We expect that the SHOE amplitude (B_{oS}) and the extent to which the grains are backward or forward scattering are mutually related to the transparency of the regolith grains. The effective asymmetry factor g_{eff} of the SPPF is a measure of the average regolith grain scattering asymmetry and is the average cosine of the scattering angle, $\Theta = \pi - \alpha$, such that

$$g_{eff} = \langle \cos \Theta \rangle = \langle -\cos \alpha \rangle = -bc$$
$$= -\frac{1}{2} \int_0^\pi P(\alpha; b, c) \cos \alpha \sin \alpha \, d\alpha, \qquad (6)$$

where $P(\alpha; b, c)$ is the SPPF from Equation (4). g_{eff} is negative for backscattering grains, positive for forward-scattering grains, and zero for symmetrically scattering grains. B_{oS} is a direct measure of grain transparency, with values ranging from $B_{oS} = 0$ for perfectly transparent grains to $B_{oS} = 1$ for opaque

grains. Grains can be opaque if they are composed of an absorbing material or if they contain a high density of internal scatterers (see Figure 8), or both.

Figure 9 shows the relationships between B_{oS} and g_{eff} for the DPs and DKBOs, which can best be interpreted with the help of Figure 8. The presence of absorbing regolith materials on Ixion and OE$_{394}$, as indicated by their low values of $\tilde{\omega}_o$ (Table 14), plays an important role, together with the presence of a high density of internal scatterers, in making their regolith grains opaque. In contrast, Charon is covered with regolith grains that have comparatively high single-scattering albedos ($\tilde{\omega}_o > 0.7$), suggesting that they are opaque primarily because of their relatively high density of internal scatterers and perhaps large grain sizes and/or aggregation.

The SHOE amplitude B_{oS} provides a test of consistency in the interpretation of grain transparency. Opaque grains produce dark shadows and yield high values of B_{oS} near unity. This behavior is represented in Figure 9(a) by nearly all of the nonvolatile regoliths and H$_2$O-rich bodies. However, transparent grains, like those on Triton and Pluto, illuminate particle shadows and hence yield lower values of B_{oS}.

The forward-scattering regolith types define a trend in Figure 9(b) that extends from approximately isotropic or symmetric examples (Haumea, Quaoar, and 2002 MS$_4$) to highly transparent grain types (Eris, Triton, Pluto, and Makemake). Quaoar and 2002 MS$_4$ have low-albedo regolith grains ($\tilde{\omega}_o < 0.7$), but also relatively low densities of internal scatterers. Haumea's regolith grains are significantly higher in albedo, and they have a higher density of internal scatterers. Unlike the other two, however, Haumea's regolith grains are less irregular in shape. The hypervolatile bodies, Triton, Pluto, Makemake, and Eris, all have grains that have very low densities of internal scatterers, very smooth shapes, and very high single-scattering albedos ($\tilde{\omega}_o > 0.94$). These characteristics mean that grains on their surfaces are very similar to terrestrial frost and snow grains (see Verbiscer & Veverka 1990; Hapke 2012a).

4.6. Regolith Structure

Three Hapke (2012b) model parameters describe structural attributes of the regolith. The macroscopic roughness parameter $\bar{\theta}$ describes surface texture typically at subdecimeter scales (see Helfenstein & Shepard 1999). The SHOE h_S parameter describes the regolith porosity and packing of grains. Finally, the b parameter of the McGuire & Hapke (1995) SPPF describes the regolith grain shape and roughness. Although each attribute represents a different size domain, interrelationships among them may exist, as the regolith has an aggregate architecture that encompasses these scales over the dimension range of photometric sensitivity.

It has long been established (see Buratti & Veverka 1985) that light reflected among macroscopic scale topographic relief, particularly on high-albedo surfaces, can attenuate projected shadows and amplify light reflected from adjacent facets to the observer. The effect of the multiply reflected light is to subdue the photometric signature of topographic roughness such that the photometrically detectable roughness can significantly underestimate the actual roughness. In this and many earlier studies, fits of the macroscopic roughness parameter were performed using the traditional Hapke (1984) macroscopic roughness correction that forms the basis for all subsequent incarnations of the Hapke model. The solved values of
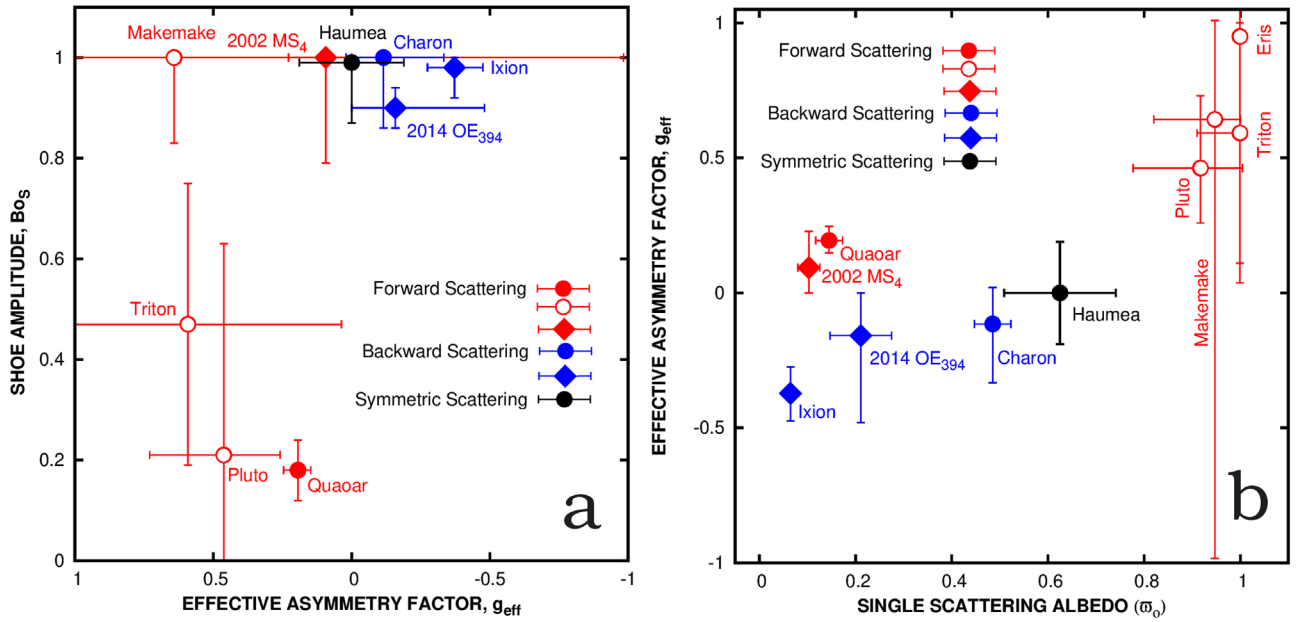
Figure 9. Relationships between transparency-related Hapke model parameters. Open circles represent hypervolatile surfaces, filled circles describe H$_2$O-rich surfaces, and diamonds represent nonvolatile surfaces or surfaces of undetermined composition. Red data points identify surfaces dominated by forward-scattering regolith grains, blue data points by backscattering grains, and black points by isotropically or symmetrically scattering grains. (a) SHOE amplitude parameter B_{oS} vs. the SPPF effective asymmetry parameter g_{eff} for DPs and large KBOs. In most cases, the SHOE is most prominent in regoliths composed of nearly opaque grains ($B_{oS} > 0.8$). Forward-scattering grains typically diminish projected shadows, resulting in low SHOE amplitudes, although Makemake appears to be an exception. (b) Relationship between the SPPF effective asymmetry parameter g_{eff} and single-scattering albedo $\tilde{\omega}_o$ suggests a trend from dominantly backscattering low-albedo particles ($g_{eff} < 0$) to dominantly forward-scattering ($g_{eff} > 0$) high-albedo grains. Hypervolatile-rich surfaces consistently have grains that are both highest in single-scattering albedo and forward scattering. Nonvolatile surfaces have low particle albedos and range from moderately backscattering to nearly isotropic or with symmetric forward- and backscattering lobes. The behavior of H$_2$O-rich surfaces tends to lie in between the hypervolatile and nonvolatile surfaces.

topographic slope angle that are reported are necessarily the *photometrically detectable* values rather than the *actual* mean physical slope angles. Hapke (2012b) introduced an as-yet-untested theoretical model that relates the photometrically detected macroscopic roughness slope angle, $\bar{\theta}_p$, to the actual slope angle, $\bar{\theta}$:

$$\bar{\theta}_p = \bar{\theta}\left(\frac{2\gamma}{1+\gamma}\right). \tag{7}$$

In the variant of this model presented in Helfenstein & Verbiscer (2022, in preparation), the correction depends on both $\tilde{\omega}_o$ and the effective asymmetry factor of the SPPF, g_{eff}, from Equation (6):

$$\gamma(\tilde{\omega}_o, g_{eff}) = \sqrt{\frac{1-\tilde{\omega}_o}{1-\tilde{\omega}_o\, g_{eff}}}. \tag{8}$$

The difference between the actual roughness and that which can be obtained from photometric observations is relatively small for dark to moderately bright surfaces, but the difference becomes nonlinearly larger as $\tilde{\omega}_o$ approaches unity. This effect is amplified if the regolith particles are backward scattering ($g_{eff} < 0$) and reduced if they are forward scattering ($g_{eff} > 0$). For extremely bright surfaces like Triton and at the upper uncertainty limits of Makemake and Pluto, the model predicts that the roughness signature is so subdued as to be undetectable. For these objects, the actual roughness may be indeterminate, at least at the upper range of measurement uncertainty (Table 17).

The uncertainty estimates for the actual values of $\bar{\theta}$ are necessarily large owing to the generally limited phase angle

coverage for the objects, which compounds the uncertainties in $\bar{\theta}_p$, g_{eff}, and $\tilde{\omega}_o$. Of the objects for which $\bar{\theta}_p$ was fixed at 20°, those with low to moderate albedos (Ixion, MS$_4$, Quaoar, and Haumea) have values of $\bar{\theta}$ that are not much different from their *photometric* roughness values. As expected, the largest variations in estimated roughness values (and uncertainties) occur for the highest-albedo objects (Eris, Makemake, Charon, Pluto, and Triton).

Figure 10(a) examines the possible relationship between particle shape and the packing of particles in the regolith. We hypothesize that rough-shaped particles (small values of b) yield a more porous regolith (small values of h_S) than smooth particles (large values of b); however, we find no clear correlation. Figure 10(b) examines the possible relationship between macroscopic roughness and particle shape. Our hypothesis here is that the arrangements of rougher-shaped particles yield macroscopically rougher regoliths (i.e., larger $\bar{\theta}$) than smoother grains. Despite some large uncertainties, the nominal data points support our hypothesis.

4.7. Phase Coefficients, Phase Integrals, and Bond Albedos

We use the Hapke (2012b) parameters in Table 14 to generate disk-integrated phase curves (solid lines in Figures 3–5) from which we measure the phase coefficients, phase integrals, and Bond albedos for each DP, satellite, and large KBO (Table 18). Phase coefficients β (phase curve slopes) are measured in two phase angle ranges: at small phase angles between $\alpha = 0°.5$ and $1°.5$ and at larger phase angles between $\alpha = 10°$ and $50°$. Most solar phase curves are relatively linear between $10°$ and $50°$; however, only Makemake, Pluto, and Triton have relatively linear phase curves between $0°.5$ and $1°.5$. Triton and Pluto have remarkably

Table 17
Corrected Macroscopic Roughness Parameter Values

Object	Photometric Roughness (deg) $\bar{\theta}_p$ [a]	g_{eff}	$\tilde{\omega}_o$	$\bar{\theta}_{\min}$	Actual Roughness (deg) $\bar{\theta}_{\mathrm{nominal}}$	$\bar{\theta}_{\max}$
Eris	$(20)^{+23}_{-20}$	$0.95^{+0.05}_{-0.84}$	$0.99\overline{9}^{+0.000}_{-0.003}$	0	[IND][b]	[IND]
Makemake	5^{+10}_{-5}	$0.64^{+0.37}_{-1.63}$	$0.947^{+0.053}_{-0.127}$	0	9	[IND]
Haumea	$(20)^{+30}_{-20}$	0.00 ± 0.19	0.625 ± 0.116	0	26	50
Quaoar	$(20)^{+23}_{-20}$	$0.19^{+0.051}_{-0.046}$	0.145 ± 0.028	0	21	45
2002 MS$_4$	$(20) \pm 2$	$0.093^{+0.093}_{-0.135}$	0.103 ± 0.023	19	21	22
Ixion	$(20)^{+30}_{-20}$	-0.37 ± 0.10	0.065 ± 0.005	0	21	51
2014 OE$_{394}$	34 ± 14	$-0.16^{+0.16}_{-0.32}$	0.211 ± 0.064	21	37	54
Triton	27 ± 9	$0.59^{+0.69}_{-0.56}$	$0.99\overline{9}^{+0.000}_{-0.089}$	19	[IND]	[IND]
Pluto	28 ± 5	$0.46^{+0.26}_{-0.20}$	$0.917^{+0.083}_{-0.140}$	28	50	[IND]
Charon	23 ± 1	$-0.012^{+0.135}_{-0.022}$	0.485 ± 0.038	26	28	47

Notes.
[a] Error bar values are rounded to nearest degree.
[b] [IND] denotes an indeterminate value because of model degeneracy for surfaces with very high albedos and strongly anisotropic particle phase functions.

similarly shaped near-opposition phase curves (Figure 4) that are relatively shallow between $0°1$ and $2°$ and rise sharply between $0°1$ and $0°$, both by ~ 0.13 mag. Makemake also has a relatively flat phase curve between $0°5$ and $1°5$ ($\beta = 0.041$ mag deg^{-1}), but without observations at $\alpha < 0°5$ we do not know if it has a Pluto/Triton-like sharp, narrow opposition surge. Makemake, like Pluto, Eris, and Triton, has a hypervolatile-rich surface, although its atmosphere, if it has one, is much thinner. A stellar occultation by Makemake placed an upper limit of $4-12$ nanobars on the pressure at its surface (Ortiz et al. 2012). Eris also has a methane-rich surface, but its near-opposition solar phase curve is steeper than that of Pluto, Triton, and Makemake, with $\beta = 0.090$ mag deg^{-1}. At larger phase angles where the phase curves are more linear between $10°$ and $50°$, Pluto, Triton, Makemake, and Eris all have remarkably similar phase coefficients, $\beta = 0.0189$, 0.0156, 0.0168, and 0.0108 mag deg^{-1}, respectively. Haumea, Quaoar, Charon, OE$_{394}$, and MS$_4$ all have steeper solar phase curves in both phase angle ranges, with phase coefficients ranging from $\beta = 0.085$ to 0.331 mag deg^{-1} between $\alpha = 0°5$ and $1°5$ and from $\beta = 0.0205$ to 0.0315 mag deg^{-1} between $\alpha = 10°$ and $50°$. Ixion has the steepest solar phase curve between $\alpha = 10°$ and $50°$ with $\beta = 0.0315$ mag deg^{-1}, and OE$_{394}$ has the steepest solar phase curve near opposition with $\beta = 0.331$ mag deg^{-1}. In a previous study, Verbiscer et al. (2019b) found that other small, dark DKBOs observed by New Horizons all had steep solar phase curves between $\alpha = 10°$ and $50°$, with phase coefficients ranging from $\beta = 0.0291$ to 0.0362 mag deg^{-1}, much like those of MS$_4$, Ixion, and Haumea.

The phase integral q is given by

$$q = 2 \int_0^\pi \Phi(\alpha) \sin \alpha \, d\alpha, \qquad (9)$$

where $\Phi(\alpha)$ is the disk-integrated reflectance normalized to unity at $\alpha = 0°$. We approximate the phase integral q using

$$q = 0.135 + 2.671 \Phi(70), \qquad (10)$$

where $\Phi(70)$ is the reflectance at $\alpha = 70°$ on the solar phase curve normalized to unity at opposition (Verbiscer & Veverka 1988). Phase integrals for these objects vary considerably, from $q = 0.34 \pm 0.06$ for Ixion to 1.04 ± 0.05

for Eris. Phase integrals for Eris and Makemake need to be interpreted with caution, however, again because neither DP has been observed at phase angles $\alpha > 32°$, and therefore their reflectance at $\alpha = 70°$ is only derived from their modeled phase curves, which do not include high-phase observations. Nevertheless, the phase integrals of Triton, Eris, and Makemake are the largest in the solar system. OE$_{394}$'s phase integral $q = 0.36 \pm 0.05$ is consistent, within the uncertainties, with those of other DKBOs observed by New Horizons (Verbiscer et al. 2019b).

The spherical or Bond albedo $A_B = p_V q_V$ is the ratio between the total flux radiated in all directions and the total incident solar flux, and as such it is a measure of the energy balance on the surface as a whole and an important planetary surface parameter. The bolometric Bond albedo is the spherical albedo integrated over all wavelengths. Bond albedos for all of these DPs and large KBOs range from $A_B = 0.037 \pm 0.007$ for Ixion to $A_B = 0.99^{+0.01}_{-0.09}$ for Eris. The larger, brighter DPs have the shallowest phase curves and therefore highest Bond albedos, while the darker, somewhat smaller objects have the lowest Bond albedos. OE$_{394}$'s Bond albedo $A_B = 0.054^{+0.040}_{-0.026}$ is consistent with those of other DKBOs observed by New Horizons, although for most of these darker, smaller DKBOs, geometric albedos are assumed to match those of the average members of their dynamical classes instead of being directly measured (Verbiscer et al. 2019b).

We examine the phase integral q_V as a function of the visible geometric albedo p_V (Figure 11) to facilitate comparisons between the surface scattering properties of the DPs and large KBOs observed by New Horizons and those of other solar system objects. The geometric albedo for OE$_{394}$ and the DKBOs studied by Verbiscer et al. (2019b) assume the values reported by Lacerda et al. (2014) for each dynamical class, so their placement along the horizontal axis in Figure 11 is only approximate.

Generally, large objects (>400 km in diameter) have higher geometric albedos and phase integrals; their phase curves are shallower than those of smaller, darker bodies. Small bodies, especially comet nuclei and small asteroids, have the steepest phase curves and lowest phase integrals and albedos
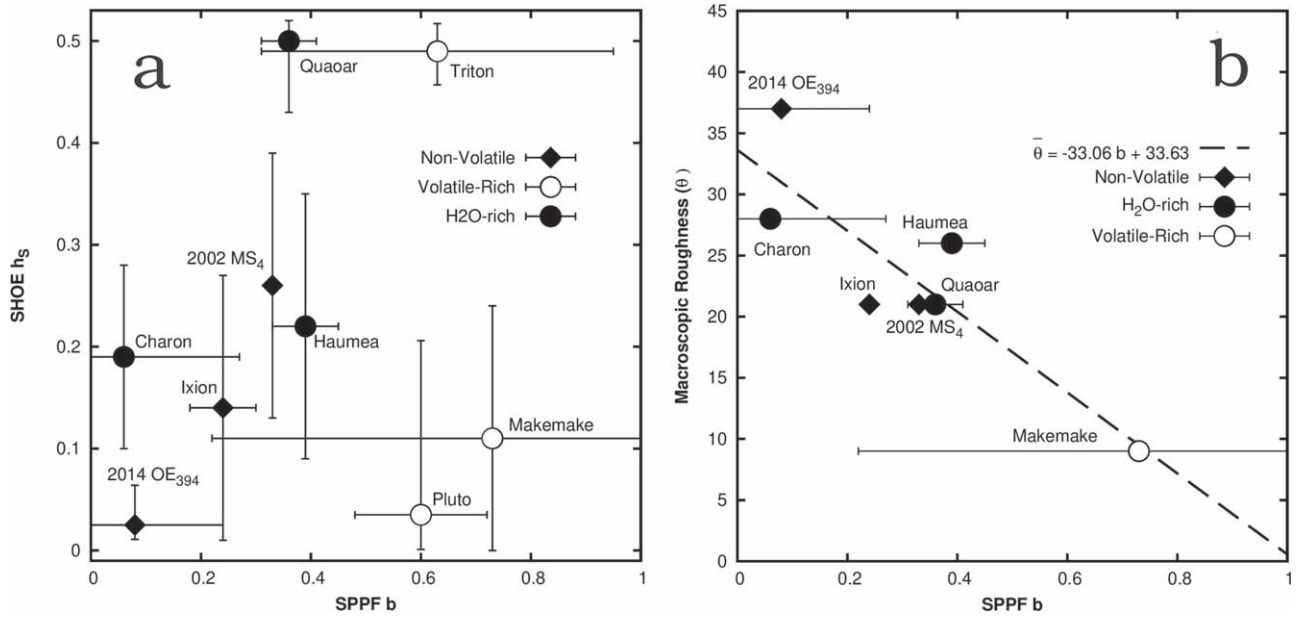
Figure 10. Relationships among texture-dependent parameters of the Hapke model ($\bar{\theta}$, h_S, and SPPF b). Open circles represent hypervolatile-rich surfaces, diamonds represent nonvolatile surfaces or those otherwise of undetermined volatile content, and filled circles represent H_2O-rich surfaces. (a) Plot of h_S vs. SPPF b shows that there is no unique correlation between the regolith porosity predicted from SHOE and the regolith grain surface roughness, indicated by the b parameter of the average SPPF. (b) Nominal corrected "actual" mean roughness slope angle values of $\bar{\theta}$ are plotted from Table 17 against the SPPF b parameter. Objects with roughness angles greater than 45° have been excluded. Vertical error bars have been omitted owing to the degeneracy of the albedo and scattering asymmetry correction at the estimated uncertainty limits in the uncorrected values of $\bar{\theta}_p$ or otherwise on bodies for which $\bar{\theta}_p$ was fixed at a constant value during fits of the Hapke model to the phase curves. The dashed line represents an (unweighted) fit to the nominal data points, $\bar{\theta} = -33.06b + 33.63$, and suggests that macroscopically smoother surfaces correlate with regolith grains that have smoother, more regular shapes.

Table 18
Phase Coefficients, Phase Integrals, and Bond Albedos for Dwarf Planets, Satellites, and Large KBOs Observed by New Horizons

Object	Phase Coefficient $\alpha = 0°.5-1°.5$ β_V (mag deg^{-1})	Phase Coefficient $\alpha = 10°-50°$ β_V (mag deg^{-1})	Phase Integral q_V[a]	Bond Albedo A_B[b]
Eris	0.090	0.0108	1.04 ± 0.05	$0.99^{+0.01}_{-0.09}$
Makemake	0.041	0.0168	0.90 ± 0.05	0.74 ± 0.06
Haumea System	0.085	0.0310	0.44 ± 0.03	0.33 ± 0.03
Quaoar	0.200	0.0217	0.52 ± 0.01	0.057 ± 0.005
2002 MS$_4$	0.158	0.0284	0.40 ± 0.03	0.039 ± 0.005
Ixion	0.129	0.0315	0.34 ± 0.06	0.037 ± 0.007
2014 OE$_{394}$	0.331	0.0205	0.36 ± 0.05	$0.054^{+0.040}_{-0.026}$
Triton	0.0080	0.0156	0.94 ± 0.04	0.81 ± 0.04
Pluto	0.0261	0.0189	0.80 ± 0.10	0.41 ± 0.06
Charon	0.0927	0.0192	0.60 ± 0.06	0.25 ± 0.04

Notes.
[a] Phase integrals q_V calculated using the approximation $q_V = 0.135 + 2.671\Phi(70)$, where $\Phi(70)$ is the normalized albedo at $\alpha = 70°$ (Verbiscer & Veverka 1988).
[b] Bond albedo $A_B = p_V q_V$ calculated using the p_V values in Table 2, except for the Haumea system $p_V = 0.75$ is applied to calculate Haumea's system Bond albedo. For 2014 OE$_{394}$, A_B assumes the average geometric albedo $p_V = 0.15$ for CCKBOs from Lacerda et al. (2014).

(Figure 11(c)). Most comet nuclei have p_V between 0.03 and 0.07 and phase integrals q_V between 0.22 and 0.3, with the exception of Comet 81P/Wild 2, which has an exceptionally low phase integral ($q = 0.16$; Li et al. 2013), due to its steep phase curve.

The DPs and large KBOs in this study have phase integrals that range from $q = 0.34 \pm 0.06$ for Ixion to $q = 1.04 \pm 0.05$ for Eris and $q = 0.90 \pm 0.05$ for Makemake. While Eris's and Makemake's phase curves are shallow and closely match the shape of Triton's ($q = 0.94 \pm 0.04$), recall that the largest phase

angles at which these DPs have been observed are $\alpha = 25°$ and $\alpha = 32°$, respectively, so clearly there is a need for additional observations of Eris and Makemake at higher phase angles to constrain their phase integrals. Quaoar and 2002 MS$_4$, however, are large KBOs with dark surfaces, and their phase integrals and geometric albedos are similar to those of the Moon and Mercury. The phase integral and geometric albedo of large Plutino Ixion are similar to those of DP Ceres and Uranus's satellite Puck. The phase integral and (assumed) geometric albedo of OE$_{394}$, and therefore the shape of its solar
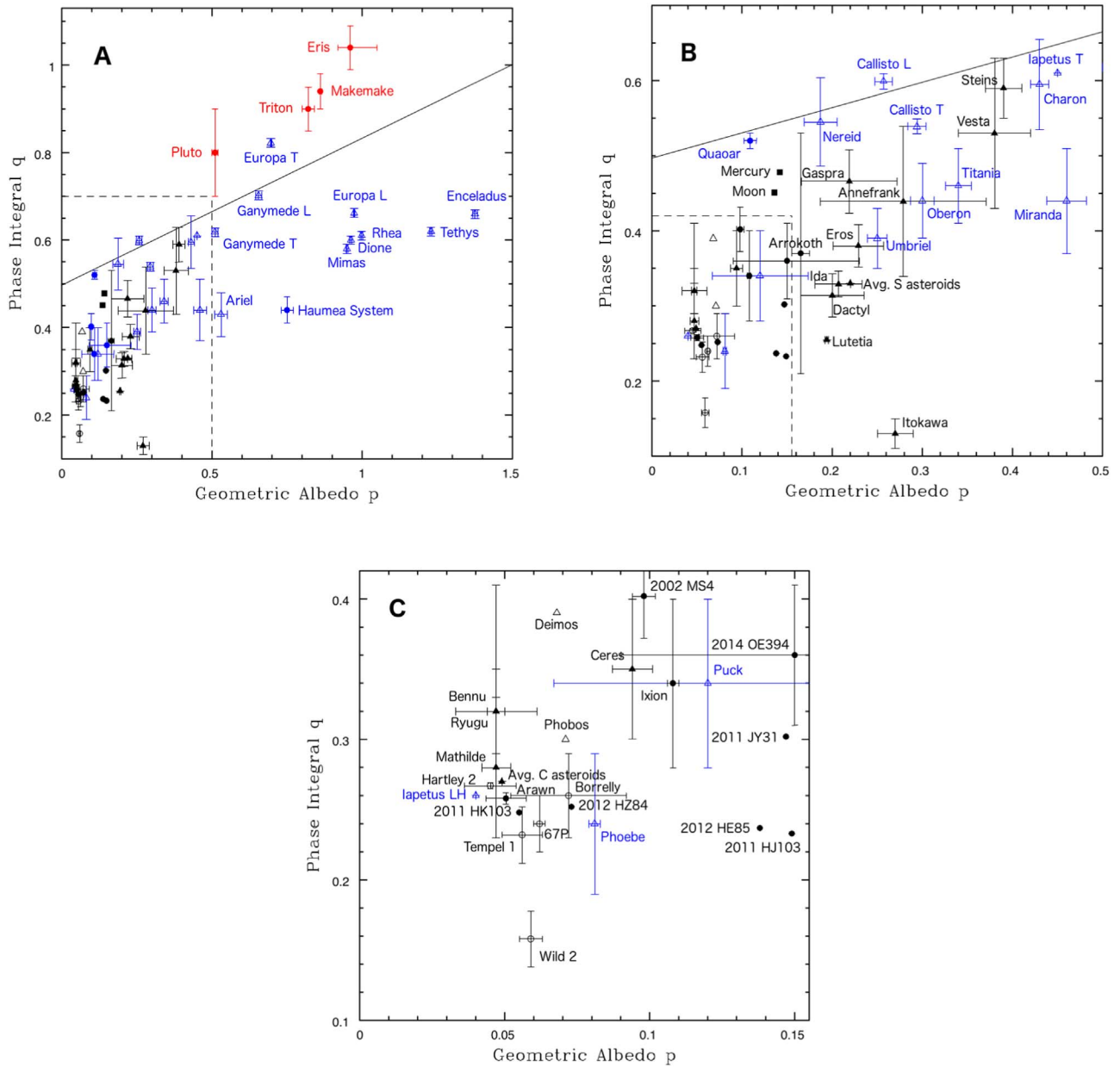
Figure 11. Phase integral q_V vs. visible geometric albedo p_V for objects in the solar system that have been observed at phase angles large enough to evaluate their phase integrals. Filled circles are KBOs; open circles are comets; open triangles are satellites; filled triangles are asteroids and Ceres. Objects with hypervolatile surface compositions are shown in red; objects on which water ice has been detected are shown in blue; objects with unknown or nonvolatile surface compositions are shown in black. L and T denote leading and trailing hemispheres, respectively. Filled squares represent the Moon and Mercury. Generally, observations at $\alpha > 70°$ are required to estimate phase integrals (Verbiscer & Veverka 1988). Panel (a) contains all objects; however, to facilitate the identification and location of objects with $p_V < 0.5$, panel (b) corresponds to the area within the box defined by the dashed lines in panel (a). Panel (c) corresponds to the area within the box defined by the dashed lines in panel (b) (i.e., those objects with $p_V < 0.15$ and $q_V < 0.4$). The solid line is the proposed Brucker et al. (2009) linear relationship between q_V and p_V; see text for discussion. Data points are shown for Triton (Hillier et al. 1990); Nereid (Thomas et al. 1991); Europa, Ganymede, Callisto (Domingue & Verbiscer 1997); Mimas, Enceladus, Tethys, Dione, Rhea (Verbiscer et al. 2007); Iapetus (Blackburn et al. 2010); Phoebe (Simonelli et al. 1999; Miller et al. 2011); Phobos (Simonelli et al. 1998); Deimos (Thomas et al. 1996); Miranda, Ariel, Umbriel, Titania, Oberon, Puck (Karkoschka 2001); Pluto, Charon (Verbiscer et al. 2019a); Mercury (Warell & Bergfors 2008); the Moon (Helfenstein & Veverka 1987); Ceres (Ciarniello et al. 2017); Vesta (Li et al. 2013); Eros (Li et al. 2004); Ida, Dactyl, Gaspra (Helfenstein et al. 1996); Mathilde (Clark et al. 1999); Lutetia (Masoumzadeh et al. 2015); Steins (Spjuth et al. 2012); Annefrank (Hillier et al. 2011); Itokawa (Tatsumi et al. 2018); Bennu (Takir et al. 2015); Ryugu (Ishiguro et al. 2014); C and S asteroids (Helfenstein & Veverka 1989); Borrelly (R band), Hartley 2, Tempel 1, Wild 2 (Li et al. 2013); 67P (Ciarniello et al. 2015); and Arrokoth (Stern et al. 2019).

phase curve, are also similar to those of Puck and 2011 JY$_{31}$, a cold classical DKBO also observed by New Horizons at high phase angles (Verbiscer et al. 2019b). All phase integrals are insensitive to p_V, since the phase integral is measured from a normalized solar phase curve; therefore, the location of OE$_{394}$ on the vertical axis is not affected by the assumption of its p_V.

Brucker et al. (2009) proposed a linear relationship between q_V and p_V ($q_V = 0.336p_V + 0.497$; solid line in Figure 11) by fitting preliminary values for several solar system objects; however, examination of updated values for both q_V and p_V demonstrates that the relationship between the two quantities is not linear for all visible geometric albedos. The Brucker et al. (2009)

approximation predicts smaller phase integrals for Eris, Makemake, Pluto, Triton, and the leading hemisphere of Europa and larger phase integrals for Haumea, Ixion, MS$_4$, OE$_{394}$, and most other solar system objects. Although the geometric albedo includes the often substantial opposition effect, even for low-albedo objects (Hapke 2021), moving points to the left to account for the opposition effect, or plotting the reflectance at $\alpha = 1°$ rather than at opposition, according to the definition of the geometric albedo, does not validate the Brucker et al. (2009) approximation for phase integrals based on albedo. Estimations of the diameters of DPs and other KBOs from their thermal emission rely on accurate estimates of their Bond albedos (see Stansberry et al. 2008; Fornasier et al. 2013) and often use the Brucker et al. (2009) approximation to estimate phase integrals and therefore Bond albedos ($A_B = p_V q_V$) from visible geometric albedos. Figure 11 shows that this approximation cannot reliably be used to estimate phase integrals and therefore Bond albedos from geometric albedos alone. The approximation overestimates phase integrals for all objects with $p_V < 0.5$ except Callisto's leading hemisphere and underestimates phase integrals for objects with surfaces dominated by hypervolatiles such as Pluto, Makemake, Triton, and Eris. The mid-sized icy satellites of Saturn have extremely high geometric albedos, due to the ongoing surface bombardment by E-ring particles (Verbiscer et al. 2007), and as a result, the Brucker et al. (2009) approximation greatly overestimates their phase integrals.

5. Correlations between Photometric Parameters and Surface Composition

Our analyses of DP and large KBO phase curves have revealed correlations between their surface composition and scattering properties, despite the fact that uncertainty estimates for fits to the Hapke (2012b) photometric model are generally large, due to the nonuniformity and varying limitations of phase angle coverage. Nevertheless, we find that the hypervolatile-rich surfaces are most distinguished from the others by the presence of regolith particles that have both very high single-scattering albedos and strongly forward-scattering behavior. Nonvolatile surfaces are composed of low-albedo particles that are moderately backward scattering to moderately forward scattering. Surfaces that have large amounts of water ice such as Haumea, Charon, and Quaoar tend to have intermediate albedos and consist of particles that scatter incident sunlight more isotropically.

At the same time, this study indicates a population of regolith components that are effectively opaque enough to cause large shadow-hiding opposition surge amplitudes. The narrow angular widths of their coherent backscatter opposition effects indicate that the hypervolatile-rich regoliths are generally immature in comparison to most of the others we examined, while the dark regoliths of nonvolatile bodies are among the most mature. Charon's moderately mature surface likely reflects that it is geologically older than Pluto's (Moore & McKinnon 2021) but possibly modified by interactions between the satellite's surface and Pluto's atmosphere (Grundy et al. 2016) rather than impact gardening, which tends to produce broad opposition effects (Hapke 2021).

Mechanical properties of the regoliths are characterized on a macroscopic scale by the roughness parameter $\bar{\theta}$, on smaller scales by the implied regolith porosity, and on a microscopic scale by grain shapes implied from the single-scattering phase functions. Within the range of parameter uncertainties, our

results did not reveal any statistically unique systematic relationships of regolith porosity with grain shape. However, this work suggests a correlation between decreasing macroscopic surface roughness and decreasing regolith grain roughness.

6. Summary

New Horizons LORRI has been observing DPs Eris, Makemake, and Haumea; large KBOs Quaoar, Ixion, 2002 MS$_4$, and 2014 OE$_{394}$; and other DKBOs throughout its 15 yr in flight, since 2007 October, 19 months after launch. These observations, acquired at viewing geometries unattainable from Earth, enable construction of the most complete solar phase curves for DPs and large KBOs to date, as well as the first rotation phase curves for Haumea and Quaoar at high solar phase angles. New Horizons has also observed Neptune's largest satellite, Triton, at a high phase angle that both complements the Voyager 2 data set and fills in a gap in Triton's solar phase curve.

Unlike the smaller, darker DKBOs observed by LORRI, the shapes of DP and large KBO solar phase curves vary greatly, indicating a diversity in the scattering properties of surface particles on the largest bodies in the Kuiper Belt, and suggesting a correlation between surface composition and phase curve shape. Objects with surface compositions dominated by hypervolatiles, Eris, Makemake, Pluto, and Triton, have shallow solar phase curves and large phase integrals and Bond albedos. Haumea, Quaoar, Charon, and 2002 MS$_4$ all have steeper solar phase curves than the objects with hypervolatile-dominated surfaces and have correspondingly smaller phase integrals and lower Bond albedos. Although the composition of 2002 MS$_4$'s surface has not been determined, the surfaces of Haumea, Quaoar, and Charon all contain large quantities of water ice. Large Plutino Ixion and large CCKBO 2014 OE$_{394}$ have the steepest phase curves, matching the shapes of the smaller, dark DKBOs observed by New Horizons, as well as those of other small, dark solar system objects, including asteroids, comets, and satellites Phobos and Phoebe.

The total amplitude of Haumea's rotation curve at $\alpha = 48°$ is 0.6 ± 0.2 mag, nearly twice that of its amplitude viewed from Earth at smaller phase angles; the increase may be due to Haumea's oblong shape or surface albedo heterogeneity, or both. The total amplitude of Quaoar's rotation curve does not increase when viewed at high solar phase angles, and whether its variation in reflectance is due to shape, topography, or surface albedo heterogeneity cannot be determined from the New Horizons observations.

As New Horizons ventures further into the Kuiper Belt, the spacecraft continues to make observations of DKBOs, and from its increasing heliocentric distance it can sample objects from new, more distant dynamical types of KBOs. Ongoing survey programs at the National Astronomical Observatory of Japan's Subaru Telescope are taking full advantage of the ultrawide (1.8 deg^2) field of view of its Hyper Suprime-Cam (HSC) to search for new New Horizons targets. Additionally, discoveries made by Pan-STARRS and the upcoming Legacy Survey of Space and Time (LSST) at the Vera Rubin Observatory will provide candidates to add to this unique data set.

Appendix
Triton and Pluto: Comparison to Previous Work

This appendix compares fits of the Hapke model to disk-integrated observations of Pluto and Triton from this work (Tables 14, 15, A1) to those of Hillier et al. (1990, 1991a, 2021) and Buratti et al. (2011). These previous studies differed from this work in several ways:

1. This work focuses exclusively on surface photometry, while each of the previous studies combined atmospheric haze models of Pluto and Triton with a version of the Hapke model to describe their surface scattering properties.
2. Each study uses a different form of the Hapke model:
   (a) To describe the multiple scattering of light in the regolith, this work uses the Hapke (2012b) anisotropic approximation, while the previous studies instead used a first-order Legendre polynomial model.
   (b) To account for the effects of surface compaction, this work and that of Hillier et al. (2021) adopt the

Helfenstein & Shepard (2011) approximation of the Hapke (2008) porosity correction; however, Buratti et al. (2011) did not use this approximation.
   (c) This work and that of Hillier et al. (2021) model the CBOE, but Buratti et al. (2011) did not model the CBOE.
   (d) To minimize the number of model parameters, previous work used the single-parameter Henyey & Greenstein (1941) SPPF (i.e., 1PHG SPPF with parameter g_{eff}) for each object's surface and haze layer; however, this work uses the McGuire & Hapke (1995) form of the two-parameter Henyey–Greenstein (2PHG) SPPF (with parameters b, c, Equation (4)) for the surfaces. The 1PHG SPPF describes unimodal curves that represent dominantly backscattering for $g_{eff} < 0$, dominantly forward scattering for $g_{eff} > 0$, and symmetric (isotropic) scattering for $g_{eff} = 0$. The 2PHG SPPF describes bimodal curves that reduce to the 1PHG SPPF for $c = -1$, $b = |g_{eff}|$ (for forward scattering) or $c = +1$, $b = |g_{eff}|$ (for backscattering).

To evaluate Triton's surface scattering properties, this work combines ground-based V-filter (Buratti et al. 2011), Voyager 2 (Hillier et al. 1990, 1991a), and New Horizons LORRI observations (Table 13) using empirically derived magnitude offsets (Table 14, footnote d) to adjust for instrumental calibration differences and to normalize all observations relative to the ground-based V-filter data. For Pluto, this work combines HST (WFC3 F555W filter; Verbiscer et al. 2019a) and New Horizons LORRI and MVIC (red filter; Hillier et al. 2021) observations, normalized to the HST data by applying a +0.47 mag offset (Table 14, footnote e).

Particles in both Triton's and Pluto's haze layers are dominantly forward scattering, and while excluding disk-integrated observations acquired at high phase angles precludes including significant contributions from the forward-scattering haze particles, doing so also eliminates the ability to characterize forward scattering from surface particles. Therefore, for Triton, this work excludes observations acquired at $\alpha > 140°$ from Voyager 2, noting that the Triton surface model in Figure 9 in Buratti et al. (2011) reasonably fits the observations up to phase angles just under $\alpha = 140°$, and for Pluto, this work excludes all New Horizons observations acquired at phase angles $\alpha > 115°$.

The most significant differences between the Hapke parameters for Pluto and Triton derived from this and previous work (Table A1) are the contrasting values of the nominal SPPF model parameters. For both Pluto and Triton, this work predicts dominantly forward-scattering regolith grains, whereas all previous works predict dominantly backscattering grains. Figure A1 (left panels) best illustrates the contrast in the nominally predicted SPPFs. Here we use the approach of Helfenstein & Shepard (2011) to use the solution Hapke parameters to invert the mean whole-disk radiance factors to values of $\tilde{\omega}_o P(\alpha)$ and plot them with the corresponding predicted SPPF curves. It is important to note that this method assumes that all of the parameter uncertainties are compounded in the inverted values of $\tilde{\omega}_o P(\alpha)$. Figure A1 also shows the predicted SPPF curves for the corresponding haze particles.

For Pluto, the larger deviations between the data points and this work's solution, compared to those of the Hillier et al. (2021) fit, suggest that, at least for the Pluto data set, the exact first-order Legendre polynomial multiple scattering model used

Table A1
Comparison of Average Whole-disk Hapke (2012b) Parameters for Pluto and Triton

Object	Single-scattering Albedo $\tilde{\omega}_o$	Photometric Roughness $\bar{\theta}_p$ (deg)	SPPF b	SPPF c	SHOE Width h_S	SHOE Amplitude B_{oS}	CBOE Width h_C	CBOE Amplitude B_{oC}	References
Triton surface	$0.999^{+0.000}_{-0.089}$	27 ± 9	0.63 ± 0.32	$-0.94^{+0.82}_{-0.41}$	$0.495^{+0.027}_{-0.033}$	0.47 ± 0.28	$0.00055^{+0.00566}_{-0.00024}$	0.17 ± 0.04	This work
	0.998	14	0.32	$[+1]$[a]	0.0065	0.22	$\cdots$	$\cdots$	Buratti et al. (2011)
Pluto surface	$0.917^{+0.083}_{-0.140}$	28 ± 5	0.60 ± 0.12	-0.77 ± 0.23	$0.035^{+0.172}_{-0.003}$	$0.21^{+0.42}_{-0.21}$	$0.00014^{+0.00023}_{-0.00000}$	0.18 ± 0.13	This work
	$0.95^{+0.02}_{-0.26}$	19^{+3}_{-2}	$0.21^{+0.03}_{-0.01}$	$[+1]$	0.108	$0.33^{+0.09}_{-0.12}$	$0.00030^{+0.00116}_{-0.00030}$	$[1.00]$	Hillier et al. (2021)
Triton haze	$1.00^{+0.00}_{-0.02}$	$\cdots$	0.63 ± 0.12	$[-1]$	$\cdots$	$\cdots$	$\cdots$	$\cdots$	Hillier et al. (1990)
Pluto haze	$[0.94]$	$\cdots$	0.86 ± 0.02	$[-1]$	$\cdots$	$\cdots$	$\cdots$	$\cdots$	Hillier et al. (2021)

Note.
[a] Values within brackets denote the SPPF c parameter for cases that reduce to the single-parameter Henyey & Greenstein (1941) SPPF.
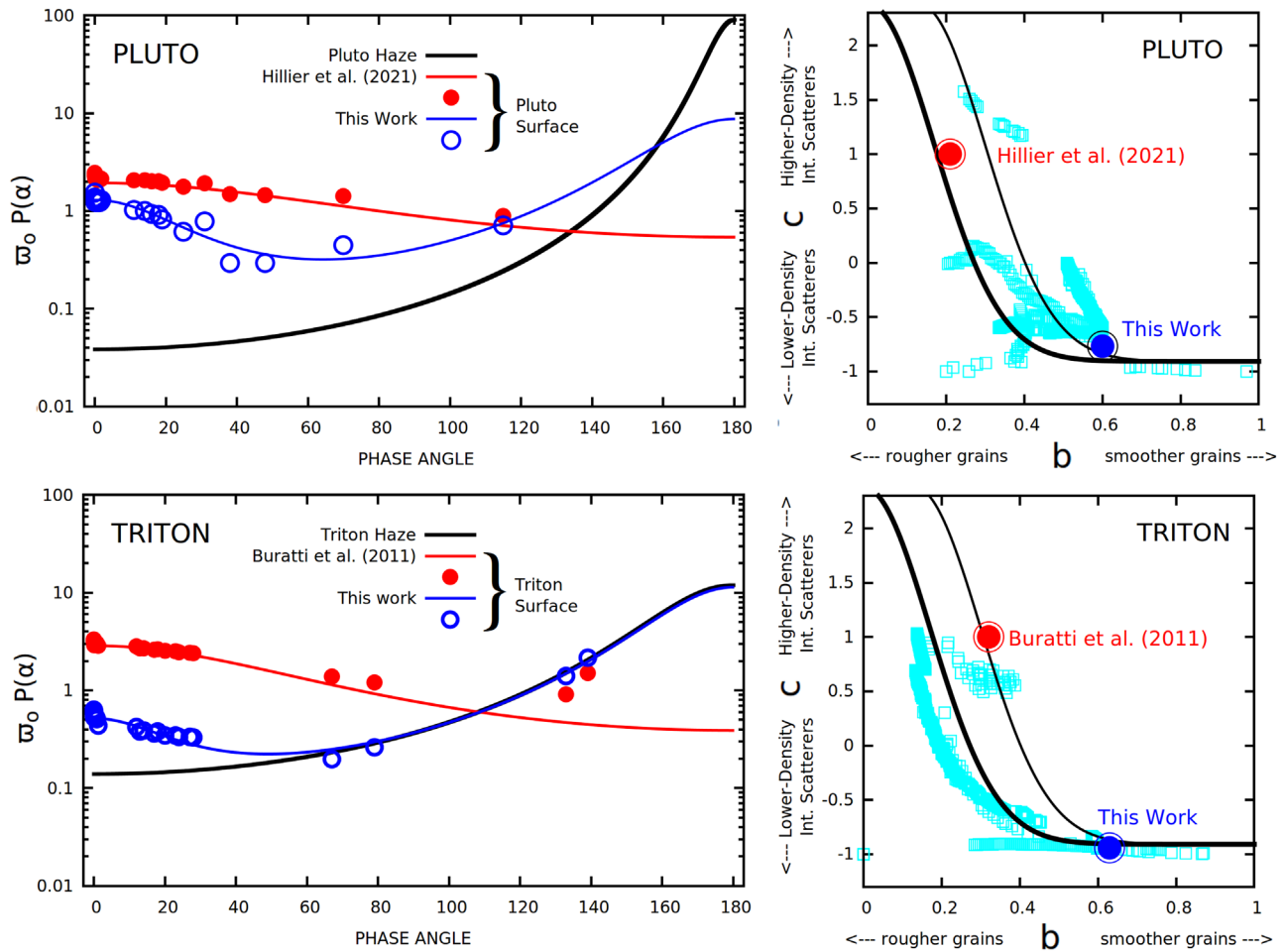
Figure A1. Comparison of retrieved global-average SPPFs for Pluto (top row) and Triton (bottom row) from this study and previous work listed in Table A1. Plots on the left show $\tilde{\omega}_o P(\alpha)$ vs. α curves predicted by the best-fit Hapke model fits from this study and from previous work. Data points are the whole-disk phase curve observations that have been inverted to corresponding values of $\tilde{\omega}_o P(\alpha)$ using the method of Helfenstein & Shepard (2011). The solid black $\tilde{\omega}_o P(\alpha)$ curves are the haze models from previous work. Plots on the right are McGuire & Hapke (1995) hockey stick plots (with thick and thin solid curves as described in the caption to Figure 8) that compare the SPPF b and c values from this study to the corresponding values from Table A1 in the context of corresponding regolith grain properties. Note that the error bars for the Hillier et al. (2021) Pluto data are smaller than the data point symbols. The cyan squares are the results of stepwise grid searches of parameter space around the best-fit solution in this work; they are the b and c values from all valid model solutions found within the nominal error envelope of the Hapke model solutions presented herein. See text for discussion.

by Hillier et al. (2021) provided a better fit than the Hapke (2012b) anisotropic multiple-scattering approximation. The shape of the forward-scattering lobe in this work is significantly broader than that of the haze layer, which suggests that our model is correctly separating the surface scattering from that of the haze layer. The Kutsop et al. (2021) investigation of Pluto's haze layer revealed that bimodal or even trimodal model SPPFs represent its phase curves at MVIC wavelengths better than the unimodal 1PHG, so that the contribution of scattered light from the haze layer may be significant even at phase angles $\alpha < 90°$ (see Triton discussion below).

For Triton, the scatter between the data points and our solution is much less than it is for Pluto. However, in this case there is good evidence that significant contributions of light scattered by the haze layer contaminated the measurements in spite of the limits imposed on the phase angle coverage. The first indication, from Table A1, is that the SPPF b parameter, the angular width of the forward-scattering lobe, is almost identical to that of the haze layer, as more dramatically shown in Figure A1. The second indication is the way that the inverted data from Buratti et al. (2011) (red points) progressively increase above the red curve with increasing phase angle. Our applied empirical corrections for

calibration differences among different observation instruments (Table 14, footnote d) may have revealed a larger difference between the scattering behavior of the haze layer and the surface of Triton than was previously detected.

Because the error bars are generally large in these cases, it is likely that the parameter values of previous work fall within the range of parameters that are statistically equivalent to this work. The right panels of Figure A1 examine this possibility by comparing the SPPF b, c parameters in the context of McGuire & Hapke (1995) hockey stick plots (as in Figure 8). It is important to note that, because previous works adopted a 1PHG SPPF, their only options for the c parameter are $c = +1$ for unimodal backscattering or $c = -1$ for unimodal forward scattering. Their choice to fit a backscattering SPPF to the surface and a forward-scattering SPPF to the haze layer avoids the ambiguity between the two mechanisms. However, this excludes the possibility that a surface composed of bright ice particles can exhibit both forward- and backscattering lobes, as our solutions suggest.

In Figure A1, the cyan points represent all valid solutions within the error envelopes found in the uncertainty analysis performed in this work. For both Pluto and Triton, there are
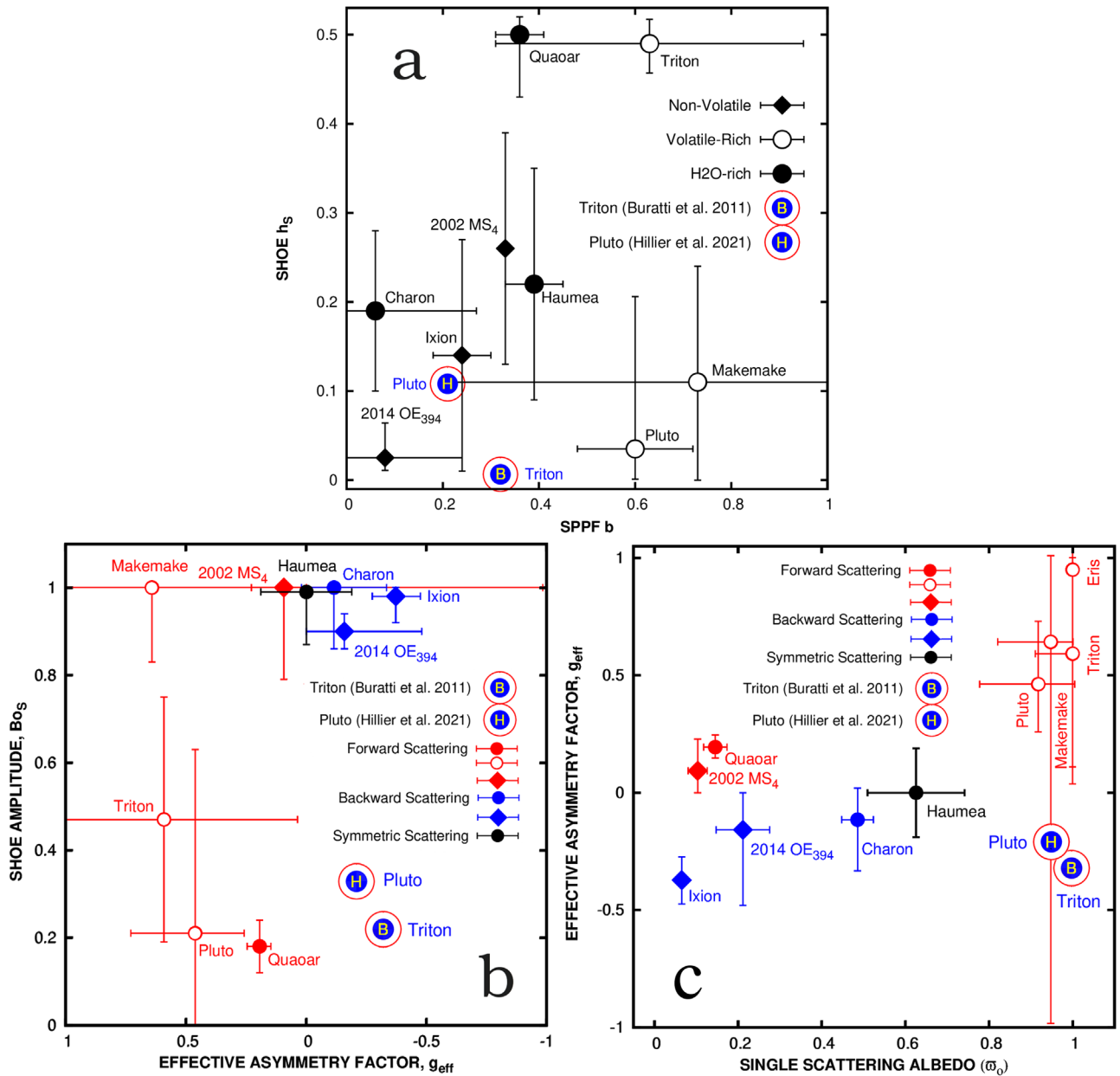
Figure A2. Placement of Pluto and Triton parameters from previous work (Table A1) in Figures 9 and 10(a). As in those figures, open circles represent volatile-rich surfaces, diamonds represent nonvolatile surfaces or those otherwise of undetermined volatile content, and filled circles represent H_2O-rich surfaces. (a) Plot of h_S vs. SPPF b shows that there is no unique correlation between the regolith porosity predicted from SHOE and the regolith grain surface roughness, indicated by the SPPF b parameter. From this work, the diagram indicates that the SPPFs of bright, volatile-rich bodies have narrower lobes than those of the darker nonvolatile and H_2O-rich bodies. However, for both Pluto and Triton, previous work found SPPFs with broad lobes, in the range of those for darker objects. (b) SHOE amplitude parameter B_{oS} vs. the SPPF effective asymmetry parameter g_{eff} for DPs and large KBOs. In most cases, the SHOE is most prominent for regoliths containing nearly opaque grains ($B_{oS} > 0.8$) that project dark shadows. Forward-scattering grains diminish projected shadows, consistent with our solutions for Triton, Pluto, and Quaoar. Previous solutions for Pluto and Triton have the low-amplitude SHOE of bright icy particles, but they imply more strongly backscattering regolith grains. (c) Relationship between the SPPF effective asymmetry parameter g_{eff} vs. $\tilde{\omega}_o$ suggests a trend from dominantly backscattering low-albedo particles to dominantly forward-scattering high-albedo grains. Solutions for volatile-rich surfaces from this work consistently have grains that are highest in both single-scattering albedo and forward scattering. Nonvolatile surface particles have low single-scattering albedos and range from moderately backscattering to nearly isotropic, with symmetric forward- and backscattering lobes. The directional scattering behavior of H_2O-rich surfaces tends to lie in between that of the hypervolatile and nonvolatile surfaces. Previous results deviate from this trend—although they have high albedos, they have asymmetry factors that are most similar to those of the darkest surfaces with the most opaque grains.

examples that fall close to, but do not match, the same b and c values as those obtained in previous work. Moreover, those that are close are at the very limits of the error envelope by 3σ.

As discussed in Section 4.3, placement of b and c parameters for Triton and Pluto on the hockey stick plots infers regolith particles that are smooth in shape and have a low density of internal scatterers or are translucent to moderately transparent.

The placement of b and c from previous work on the plots infers regolith grains with rougher, more irregular shapes and that have relatively high densities of internal scatterers, making them less transparent than found in this study.

Figures 9 and 10(a) provide context for further comparison and are reproduced in Figure A2, where additional data points represent previous results from Table A1. In summary, for

Triton and Pluto, this work infers the presence of high-albedo, transparent regolith grains that have relatively smooth or euhedral shapes. On Pluto, regolith grains form a relatively fluffy, high-porosity surface, in comparison to Triton, where they would be embedded in a denser regolith.

This work, along with previous studies, derives high single-scattering albedos for grains in both Triton's and Pluto's regolith; however, other grain properties implied from previous work are different. Previous solutions for both Triton and Pluto imply rougher grains with irregular shapes that are relatively opaque. This work concludes that Pluto's regolith is relatively fluffy with high porosity ($92^{+08}_{-28}\%$), in broad agreement with the porosity found for Pluto (78%) by Hillier et al. (2021). Buratti et al. (2011) found that Triton's porosity (98%) is much higher than that found in this work (41% ± 2%). We note, however, that since Buratti et al. (2011) did not model the CBOE, it is likely that in their solution the SHOE function mimicked Triton's very narrow CBOE and implied a high porosity. On the other hand, the broad SHOE and implied lower porosity for Triton's regolith from this work may be significantly masked by haze effects that were not completely eliminated in this analysis, perhaps leading to an underestimate in porosity.

ORCID iDs

Anne J. Verbiscer ⓘ https://orcid.org/0000-0002-3323-9304
Simon B. Porter ⓘ https://orcid.org/0000-0003-0333-6055
Susan D. Benecchi ⓘ https://orcid.org/0000-0001-8821-5927
J. J. Kavelaars ⓘ https://orcid.org/0000-0001-7032-5255
Tod R. Lauer ⓘ https://orcid.org/0000-0003-3234-7247
Jinghan Peng ⓘ https://orcid.org/0000-0002-9183-9279
Silvia Protopapa ⓘ https://orcid.org/0000-0001-8541-8550
S. Alan Stern ⓘ https://orcid.org/0000-0001-5018-7537
Harold A. Weaver ⓘ https://orcid.org/0000-0003-0951-7762
Marc W. Buie ⓘ https://orcid.org/0000-0003-0854-745X
Bonnie J. Buratti ⓘ https://orcid.org/0000-0002-5901-4875
Catherine B. Olkin ⓘ https://orcid.org/0000-0002-5846-716X
Joel Parker ⓘ https://orcid.org/0000-0002-3672-0603
Kelsi N. Singer ⓘ https://orcid.org/0000-0003-3045-8445
Leslie A. Young ⓘ https://orcid.org/0000-0002-7547-3967

References

Agnor, C. B., & Hamilton, D. P. 2006, Natur, 441, 192
Alvarez-Candal, A., Pinilla-Alonso, N., Licandro, J., et al. 2011, A&A, 532, A130
Alvarez-Candal, A., Pinilla-Alonso, N., Ortiz, J. L., et al. 2016, A&A, 586, A155
Andrae, R. 2010, arXiv:1009.2755
Andrae, R., Schulze-Hartung, T., & Melchior, P. 2010, arXiv:1012.3754
Barkume, K. M., Brown, M. E., & Schaller, E. L. 2006, ApJL, 640, L87
Barkume, K. M., Brown, M. E., & Schaller, E. L. 2008, AJ, 135, 55
Barucci, M. A., Dalle Ore, C. M., Perna, D., et al. 2015, A&A, 584, A107
Belskaya, I., Bagnulo, S., Muinonen, K., et al. 2008, A&A, 479, 265
Benecchi, S. D., Borncamp, D., Parker, A. H., et al. 2019, Icar, 334, 22
Betoule, M., Marriner, J., Regnault, N., et al. 2013, A&A, 552, A124
Blackburn, D. G., Buratti, B. J., Ulrich, R., & Mosher, J. A. 2010, Icar, 209, 738
Boehnhardt, H., Bagnulo, S., Muinonen, K., et al. 2004, A&A, 415, L21
Braga-Ribas, F., Sicardy, B., Ortiz, J. L., et al. 2013, ApJ, 773, 26
Braga-Ribas, F., Sicardy, B., Ortiz, J. L., et al. 2014, Natur, 508, 72
Brown, M. E. 2008, in The Solar System Beyond Neptune, ed. M. A. Barucci (Tucson, AZ: Univ. Arizona Press), 335
Brown, M. E. 2013, ApJL, 767, L7
Brown, M. E., Barkume, K. M., Blake, G. A., et al. 2007a, AJ, 133, 284
Brown, M. E., Barkume, K. M., Ragozzine, D., & Schaller, E. L. 2007b, Natur, 446, 294
Brown, M. E., Bouchez, A. H., Rabinowitz, D., et al. 2005a, ApJL, 632, L45

Brown, M. E., & Butler, B. J. 2018, AJ, 156, 164
Brown, M. E., Schaller, E. L., & Blake, G. A. 2015, AJ, 149, 105
Brown, M. E., & Suer, T. A. 2007, IAUC, 8812, 1
Brown, M. E., & Trujillo, C. A. 2004, AJ, 127, 2413
Brown, M. E., Trujillo, C. A., & Rabinowitz, D. L. 2005b, ApJL, 635, L97
Brown, M. E., van Dam, M. A., Bouchez, A. H., et al. 2006, ApJL, 639, L43
Brucker, M. J., Grundy, W. M., Stansberry, J. A., et al. 2009, Icar, 201, 284
Buie, M. W., Grundy, W. M., Young, E. F., Young, L. A., & Stern, S. A. 2010, AJ, 139, 1117
Buratti, B. J., Bauer, J. M., Hicks, M. D., et al. 2011, Icar, 212, 835
Buratti, B. J., & Veverka, J. 1985, Icar, 64, 320
Busso, G., Cacciari, C., Carrasco, J. M., et al. 2018, Gaia DR2 Documentation, European Space Agency; Gaia Data Processing and Analysis Consortium, https://gea.esac.esa.int/archive/documentation/GDR2/
Carraro, G., Maris, M., Bertin, D., & Parisi, M. G. 2006, A&A, 460, L39
Chambers, K. C., Magnier, E. A., Metcalfe, N., et al. 2016, arXiv:1612.05560
Cheng, A. F., Weaver, H. A., Conard, S. J., et al. 2008, SSRv, 140, 189
Ciarniello, M., Capaccioni, F., Filacchione, G., et al. 2015, A&A, 583, A31
Ciarniello, M., De Sanctis, M. C., Ammannito, E., et al. 2017, A&A, 598, A130
Clark, B. E., Veverka, J., Helfenstein, P., et al. 1999, Icar, 140, 53
Cruikshank, D. P., Roush, T. L., Owen, T. C., et al. 1993, Sci, 261, 742
Dalle Ore, C. M., Barucci, M. A., Emery, J. P., et al. 2009, A&A, 501, 349
Davis, A. B., Pasachoff, J. M., Babcock, B. A., et al. 2014, AAS Meeting, 223, 247.08
DeMeo, F. E., Fornasier, S., Barucci, M. A., et al. 2009, A&A, 493, 283
Denk, T., & Mottola, S. 2019, Icar, 322, 80
Domingue, D., & Verbiscer, A. 1997, Icar, 128, 49
Doressoundiram, A., Peixinho, N., de Bergh, C., et al. 2002, AJ, 124, 2279
Doressoundiram, A., Peixinho, N., Moullet, A., et al. 2007, AJ, 134, 2186
Duffard, R., Ortiz, J. L., Santos Sanz, P., et al. 2008, A&A, 479, 877
Dumas, C., Merlin, F., Barucci, M. A., et al. 2007, A&A, 471, 331
Dunham, E. T., Desch, S. J., & Probst, L. 2019, ApJ, 877, 41
Fornasier, S., Lellouch, E., Müller, T., et al. 2013, A&A, 555, A15
Fukugita, M., Ichikawa, T., Gunn, J. E., et al. 1996, AJ, 111, 1748
Gaia Collaboration, Brown, A. G. A., Vallenari, A., et al. 2016, A&A, 595, A2
Gaia Collaboration, Brown, A. G. A., Vallenari, A., et al. 2018, A&A, 616, A1
Galiazzo, M., de la Fuente Marcos, C., de la Fuente Marcos, R., et al. 2016, Ap&SS, 361, 212
Gehrels, T. 1956, ApJ, 123, 331
Gladman, B., Marsden, B. G., & Vanlaerhoven, C. 2008, in The Solar System Beyond Neptune, ed. M. A. Barucci et al. (Tucson, AZ: Univ. Arizona Press), 43
Grundy, W. M., Cruikshank, D. P., Gladstone, G. R., et al. 2016, Natur, 539, 65
Hainaut, O. R., Boehnhardt, H., & Protopapa, S. 2012, A&A, 546, A115
Hapke, B. 1984, Icar, 59, 41
Hapke, B. 2008, Icar, 195, 918
Hapke, B. 2012a, Icar, 221, 1079
Hapke, B. 2012b, Theory of Reflectance and Emittance Spectroscopy (2nd ed.; Cambridge: Cambridge Univ. Press)
Hapke, B. 2021, Icar, 354, 114105
Heinze, A. N., & de Lahunta, D. 2009, AJ, 138, 428
Helfenstein, P. 1986, PhD thesis, Brown Univ.
Helfenstein, P., & Shepard, M. K. 1999, Icar, 141, 107
Helfenstein, P., & Shepard, M. K. 2011, Icar, 215, 83
Helfenstein, P., Ververka, J., & Thomas, P. C. 1988, Icar, 74, 231
Helfenstein, P., & Veverka, J. 1987, Icar, 72, 342
Helfenstein, P., & Veverka, J. 1989, in Asteroids II, ed. R. P. Binzel, T. Gehrels, & M. S. Matthews (Tucson, AZ: Univ. Arizona Press), 557
Helfenstein, P., Veverka, J., & Hillier, J. 1997, Icar, 128, 2
Helfenstein, P., Veverka, J., Thomas, P. C., et al. 1996, Icar, 120, 48
Henyey, L. G., & Greenstein, J. L. 1941, ApJ, 93, 70
Hillier, J., Helfenstein, P., Verbiscer, A., et al. 1990, Sci, 250, 419
Hillier, J., Helfenstein, P., Verbiscer, A., & Veverka, J. 1991a, JGR, 96, 19203
Hillier, J., Veverka, J., Helfenstein, P., & McEwen, A. 1991b, JGR, 96, 19211
Hillier, J. H., Buratti, B. J., Hofgartner, J. D., et al. 2021, PSJ, 2, 11
Hillier, J. K., Bauer, J. M., & Buratti, B. J. 2011, Icar, 211, 546
Holler, B., Verbiscer, A., & Tegler, S. 2019, EPSC-DPS Joint Meeting, EPSC-DPS2019-961
Holler, B. J., Benecchi, S., Mommert, M., & Bauer, J. 2020, AAS/DPS Meeting, 52, 307.06
Howett, C., Olkin, C., Protopapa, S., et al. 2021, in The Pluto System After New Horizons, ed. S. Stern, L. Young, & R. Dotson (Tucson, AZ: Univ. Arizona Press), 413
Hromakina, T. A., Belskaya, I. N., Krugly, Y. N., et al. 2019, A&A, 625, A46

Ishiguro, M., Kuroda, D., Hasegawa, S., et al. 2014, ApJ, 792, 74
Jewitt, D. C., & Luu, J. 2004, Natur, 432, 731
Karkoschka, E. 2001, Icar, 151, 51
Kostov, A., & Bonev, T. 2018, BlgAJ, 28, 3
Kretlow, M. 2019, JOA, 9, 11
Kutsop, N. W., Hayes, A. G., Buratti, B. J., et al. 2021, PSJ, 2, 91
Lacerda, P., Fornasier, S., Lellouch, E., et al. 2014, ApJL, 793, L2
Lacerda, P., Jewitt, D., & Peixinho, N. 2008, AJ, 135, 1749
Lellouch, E., Kiss, C., Santos-Sanz, P., et al. 2010, A&A, 518, L147
Levine, S. E., Zuluaga, C. A., Person, M. J., et al. 2021, AJ, 161, 210
Li, J., A'Hearn, M. F., & McFadden, L. 2003, AAS/DPS Meeting, 35, 959
Li, J., A'Hearn, M. F., & McFadden, L. A. 2004, Icar, 172, 415
Li, J.-Y., Besse, S., A'Hearn, M. F., et al. 2013, Icar, 222, 559
Licandro, J., Ghinassi, F., & Testi, L. 2002, A&A, 388, L9
Licandro, J., Grundy, W. M., Pinilla-Alonso, N., & Leisy, P. 2006a, A&A, 458, L5
Licandro, J., Pinilla-Alonso, N., Pedani, M., et al. 2006b, A&A, 445, L35
Lim, T. L., Stansberry, J., Müller, T. G., et al. 2010, A&A, 518, L148
Lin, H. W., Wu, Y. L., & Ip, W. H. 2007, AdSpR, 40, 238
Lockwood, A. C., Brown, M. E., & Stansberry, J. 2014, EM&P, 111, 127
Lorenzi, V., Pinilla-Alonso, N., & Licandro, J. 2015, A&A, 577, A86
Lu, X.-P., & Jewitt, D. 2019, AJ, 158, 220
Masoumzadeh, N., Boehnhardt, H., Li, J.-Y., & Vincent, J. B. 2015, Icar, 257, 239
McGuire, A. F., & Hapke, B. W. 1995, Icar, 113, 134
Merlin, F., Alvarez-Candal, A., Delsanti, A., et al. 2009, AJ, 137, 315
Miller, C., Verbiscer, A. J., Chanover, N. J., Holtzman, J. A., & Helfenstein, P. 2011, Icar, 212, 819
Moore, J. M., & McKinnon, W. B. 2021, AREPS, 49, 173
Muinonen, K. 1990, Light Scattering by Inhomogeneous Media: Backward Enhancement and Reversal of Linear Polarization (Helsinki: Helsinki Univ.)
Nimmo, F., Umurhan, O., Lisse, C. M., et al. 2017, Icar, 287, 12
Olkin, C., Howett, C., Protopapa, S., et al. 2021, in The Pluto System After New Horizons, ed. S. Stern, L. Young, & R. Dotson (Tucson, AZ: Univ. Arizona Press), 147
Ortiz, J. L., Gutiérrez, P. J., Sota, A., Casanova, V., & Teixeira, V. R. 2003, A&A, 409, L13
Ortiz, J. L., Santos-Sanz, P., Sicardy, B., et al. 2017, Natur, 550, 219
Ortiz, J. L., Sicardy, B., Braga-Ribas, F., et al. 2012, Natur, 491, 566
Parker, A. H., Buie, M. W., Grundy, W. M., & Noll, K. S. 2016, ApJL, 825, L9
Pasachoff, J. M., Babcock, B. A., Davis, A. B., et al. 2013, AAS/DPS Meeting, 45, 310.01
Peng, J., Kavelaars, J., Fraser, W., et al. 2020, AAS Meeting, 235, 438.09
Peng, J. J. 2022, PhD thesis, Univ. Victoria
Perna, D., Hromakina, T., Merlin, F., et al. 2017, MNRAS, 466, 3594
Person, M. J., Elliot, J. L., Bosh, A. S., et al. 2011, AAS Meeting, 218, 224.12
Pinilla-Alonso, N., Brunetto, R., Licandro, J., et al. 2009, A&A, 496, 547
Porter, S. B., Buie, M. W., Parker, A. H., et al. 2018, AJ, 156, 20
Porter, S. B., Spencer, J. R., Benecchi, S., et al. 2016, ApJL, 828, L15
Protopapa, S., Grundy, W. M., Reuter, D. C., et al. 2017, Icar, 287, 218
Protopapa, S., Olkin, C. B., Grundy, W. M., et al. 2020, AJ, 159, 74
Rabinowitz, D., Baltay, C., Emmet, W., et al. 2003, AAS Meeting, 203, 38.12
Rabinowitz, D. L., Barkume, K., Brown, M. E., et al. 2006, ApJ, 639, 1238
Rabinowitz, D. L., Schaefer, B. E., Schaefer, M., & Tourtellotte, S. W. 2008, AJ, 136, 1502
Rabinowitz, D. L., Schaefer, B. E., & Tourtellotte, S. W. 2007, AJ, 133, 26

Ragozzine, D., & Brown, M. E. 2009, AJ, 137, 4766
Regnault, N., Conley, A., Guy, J., et al. 2009, A&A, 506, 999
Reuter, D. C., Stern, S. A., Scherrer, J., et al. 2008, SSRv, 140, 129
Roe, H. G., Pike, R. E., & Brown, M. E. 2008, Icar, 198, 459
Rommel, F. L., Braga-Ribas, F., Periera, C., et al. 2020, Europlanet Science Congress, 14, EPSC2020-866
Rousselot, P., & Petit, J. 2010, AAS/DPS Meeting, 42, 40.19
Sallum, S., Brothers, T., Elliot, J. L., et al. 2011, AAS Meeting, 218, 224.13
Schaefer, B. E., Rabinowitz, D. L., & Tourtellotte, S. W. 2009, AJ, 137, 129
Schaller, E. L., & Brown, M. E. 2007, ApJL, 670, L49
Sheppard, S. S. 2007, AJ, 134, 787
Sheppard, S. S., & Jewitt, D. C. 2003, EM&P, 92, 207
Shkuratov, I. G. 1988, KFNT, 4, 33
Sicardy, B., Ortiz, J. L., Assafin, M., et al. 2011, Natur, 478, 493
Simonelli, D. P., Kay, J., Adinolfi, D., et al. 1999, Icar, 138, 249
Simonelli, D. P., Wisz, M., Switala, A., et al. 1998, Icar, 131, 52
Snodgrass, C., Carry, B., Dumas, C., & Hainaut, O. 2010, A&A, 511, A72
Spjuth, S., Jorda, L., Lamy, P. L., Keller, H. U., & Li, J. Y. 2012, Icar, 221, 1101
Stansberry, J., Grundy, W., Brown, M., et al. 2008, in The Solar System Beyond Neptune, ed. M. A. Barucci et al. (Tucson, AZ: Univ. Arizona Press), 161
Stern, S. A., Bagenal, F., Ennico, K., et al. 2015, Sci, 350, aad1815
Stern, S. A., Weaver, H. A., Moore, J., et al. 2007, AAS/DPS Meeting, 39, 15.01
Stern, S. A., Weaver, H. A., Spencer, J. R., et al. 2019, Sci, 364, aaw9771
Takir, D., Clark, B. E., Drouet d'Aubigny, C., et al. 2015, Icar, 252, 393
Tatsumi, E., Domingue, D., Hirata, N., et al. 2018, Icar, 311, 175
Tegler, S. C., Grundy, W. M., Romanishin, W., et al. 2007, AJ, 133, 526
Tegler, S. C., Grundy, W. M., Vilas, F., et al. 2008, Icar, 195, 844
Tegler, S. C., Romanishin, W., & Consolmagno, G. J., S. J. 2016, AJ, 152, 210
Thirouin, A. 2013, PhD thesis, Universidad de Granada
Thirouin, A., Ortiz, J. L., Duffard, R., et al. 2010, A&A, 522, A93
Thirouin, A., & Sheppard, S. S. 2019, AJ, 158, 53
Thomas, P., Veverka, J., & Helfenstein, P. 1991, JGR, 96, 19253
Thomas, P. C., Adinolfi, D., Helfenstein, P., Simonelli, D., & Veverka, J. 1996, Icar, 123, 536
Tonry, J. L., Stubbs, C. W., Lykke, K. R., et al. 2012, ApJ, 750, 99
Trujillo, C. A., & Brown, M. E. 2003, EM&P, 92, 99
Verbiscer, A., French, R., Showalter, M., & Helfenstein, P. 2007, Sci, 315, 815
Verbiscer, A., & Helfenstein, P. 1998, in Astrophysics and Space Science Library, Vol. 227, Solar System Ices, ed. B. Schmitt, C. de Bergh, & M. Festou (Dordrecht: Kluwer), 157
Verbiscer, A., Showalter, M., Helfenstein, P., & Buie, M. 2019a, EPSC-DPS Joint Meeting, EPSC-DPS2019-1261
Verbiscer, A. J., Helfenstein, P., & Buratti, B. J. 2013, in Astrophysics and Space Science Library, Vol. 356, The Science of Solar System Ices, ed. M. S. Gudipati & J. Castillo-Rogez (New York: Springer), 47
Verbiscer, A. J., Peterson, D. E., Skrutskie, M. F., et al. 2006, Icar, 182, 211
Verbiscer, A. J., Porter, S., Benecchi, S. D., et al. 2019b, AJ, 158, 123
Verbiscer, A. J., & Veverka, J. 1988, Icar, 73, 324
Verbiscer, A. J., & Veverka, J. 1990, Icar, 88, 418
Vilenius, E., Kiss, C., Mommert, M., et al. 2012, A&A, 541, A94
Warell, J., & Bergfors, C. 2008, P&SS, 56, 1939
Weaver, H. A., Cheng, A. F., Morgan, F., et al. 2020, PASP, 132, 035003